FISFVIFR

Contents lists available at ScienceDirect

Journal of Sound and Vibration

journal homepage: www.elsevier.com/locate/jsvi



On a mode-matching technique for acoustic scattering by a cascade of cambered vanes



Léo Girier a, Michel Roger a, Hadrien Bériot b

^a Univ Lyon, École Centrale de Lyon, INSA Lyon, Université Claude Bernard Lyon I, CNRS, Laboratoire de Mécanique des Fluides et d'Acoustique, UMR 5509, 36 Avenue Guy de Collongue, F-69134, Écully, France

ARTICLE INFO

Keywords:
Axial-flow fan stage
Acoustic scattering
Mode-matching technique
Vane camber
Multiple-scale analysis

ABSTRACT

A two-dimensional mode-matching technique is developed to compute the scattering of an acoustic wave by a cascade of staggered and cambered vanes in subsonic regime, such as those encountered in axial-flow fan stages. Apart from the need to reproduce a more realistic geometry in analytical modeling, introducing vane camber is a relevant way of retrieving the global evolution of the mean flow away from the vanes, simply by mass-flow conservation through the expanding inter-vane channels. This prevents mean-flow discontinuity and introduces a realistic variation of the equivalent dipole sources along the vane chord. The expansion of the cross-section along the inter-vane channels, induced by curvature, is taken into account by multiple-scale analysis, assuming slow variations of the geometry. The validity of the model is assessed by extensive comparisons with high-fidelity numerical results, with and without flow. The assumptions used in the analytical model are found to be suited to modern geometries of outlet guide vanes.

1. Introduction

Understanding and predicting how noise propagates inside parts of aircraft engines is of crucial importance to reduce aircraft noise pollution. Engine manufacturers keep working on new technologies to meet important milestones, such as the European 2050 long-term strategy to achieve climate neutrality. Aircraft engines will need to drastically reduce their emissions, relying on, for example, increased bypass ratios, the open-fan concept and hydrogen as a sustainable alternative to petroleum-based fuels. Along with the reduction of greenhouse gases, noise pollution must still be reduced. Regardless of the chosen engine architecture, compressor stages remain a major noise contributor, especially the fan stage in turbofan engines [1]. The present work focuses on the modeling of sound scattering by staggered and cambered vanes to better understand sound transmission and reflection in fan and compressor stages.

The basis for the mathematical approach is a mode-matching technique, formulated for a periodic array of bifurcated waveguides. This technique is believed to have promising capabilities for application to modern turbofan engines, where high solidity and overlap are encountered in the fan stage; it could also be used for in-duct low-pressure compressor noise in open fan architectures. Mode-matching was first used in the context of electromagnetic fields by Whitehead [2] and later described in details by Mittra and Lee [3]. In the context of cascade aeroacoustics, alternative mathematical approaches seem to have been preferred in the 1970s, such as the acceleration potential [4] and the Wiener–Hopf technique [5] for instance; a review can be found in the paper

E-mail address: leo.girier@insa-lyon.fr (L. Girier).

URL: https://www.researchgate.net/profile/Leo-Girier (L. Girier).

https://doi.org/10.1016/j.jsv.2025.119473

Received 20 February 2025; Received in revised form 23 September 2025; Accepted 25 September 2025

Available online 3 October 2025

0022-460X/© 2025 The Authors. Published by Elsevier Ltd. This is an open access article under the CC BY license (http://creativecommons.org/licenses/by/4.0/).

^b Siemens Industry Software NV, Interleuvenlaan 68, 3001 Leuven, Belgium

^{*} Corresponding author.

Nomenclature

Abbreviations

FEM Finite Element Method LE/TE Leading/Trailing Edge

MMBCW Mode Matching for Bifurcated Curved Waveguides MMBW Mode Matching for Bifurcated Waveguides

Perfectly Matched Layers PML SDT Source Diagnostic Test

Greek characters

transverse wavenumber $\alpha_{j,p,q}$ β Prandtl-Glauert factor Kronecker delta δ

slow expansion parameter ϵ Γ vector of conservative variables slowly-varying axial wavenumber μ

angular frequency ω velocity potential φ normalized mode shape camber angle and stagger angle Ψ, Ψ γ stream-wise channel variation function

Latin characters

J. Y Bessel function of the first and second kind u*, U, u total, mean and fluctuating velocity

A, Bprojection coefficients between straight and curved channel modes

staggered axial wavenumber $K_{j,q,p}$

 $\mathcal{P}_{i,r,t}$ acoustic power

 $\mathfrak{I}_{q,p}$ inner product of the annular and channel modal bases

 ρ^*, D, ρ total, mean and fluctuating density $a = b \cos \Psi$ vane spacing normal to the vanes LE

 A_q , B_q downstream and upstream channel modal coefficients

vane spacing b

 c^*, C, c total, mean and fluctuating sound speed

inter-vane height h

 h_s scale factor for the coordinate s

imaginary unit $k = \omega/C$ acoustic wavenumber axial wavenumber $k_{j,p,q}$

inter-vane channel length, from interface BC to TE

 $L_c = \epsilon l_c$ inter-vane channel length expressed in the slow coordinate

M = U/CMach number

slowly-varying mode amplitude N p^*, P, p total, mean and fluctuating pressure

 R, R_c radius of the unwrapped cut, and vane curvature radius

reflected and transmitted modal coefficients R_p, T_p

curved-channel system of coordinates attached to interface BC s, n, z

 $S = \epsilon s$ slow curvilinear coordinate

number of vanes

x, y, zannular system of coordinates attached to LE vane system of coordinates attached to LE ζ, η, z x', y', z'annular system of coordinates attached to TE

 \boldsymbol{Z} acoustic impedance

Subscripts and superscripts Ohli, Propagating to the incident annular, reflected annular, downstream-propagating channel, upstream-propagating channel, or transmitted annular field Ohli, P. annular incident annular incident

by Bouley et al. [6]. The mode-matching technique received renewed interest with the works of Roger et al. [7–10], applying the method to centrifugal compressors. This approach accounts for a fully three-dimensional annular duct geometry without resorting to strips, and therefore naturally accounts for the radial scattering. More recently, Bouley et al. [6] developed a two-dimensional model of acoustic generation and transmission for axial-flow turbofan engines. The model has been extended to three dimensions for wake-interaction noise by Bouley et al. [11], and for turbulence impingement noise by Fraçnois et al. [12]. In the meantime, an alternative mode-matching approach was developed, relying on the edge-dipole theory to recover the sound otherwise produced by the impingement of vortical gusts [13]. The edge-dipole formalism was also used to model trailing-edge noise in Refs. [14,15].

In each of the aforementioned papers, the vanes are considered as infinitely thin flat plates with zero stagger, sweep and lean. Returning to two dimensions, some extensions have been made to consider more realistic vane geometries. Stagger angle was introduced by the use of Green's second identity in Ref. [16], following Mittra and Lee [3]. Roger et al. [14] were the first to include vane camber in the mode-matching technique. To do so, the inter-vane channels were modeled as straight channels with a slowly varying cross-section, which is equivalent to a low-frequency approximation of the camber effects. Good qualitative agreements have been obtained by Roger and Moreau [17] when applying the mode-matching technique with cambered vanes compared to the results of Hixon [18] produced with the NASA Glenn Research Center BASS code, which solves the fully nonlinear Euler equations. A comparative study of two-dimensional sound transmission models in realistic turbomachinery cascades, involving the mode-matching technique [14] and the Wiener-Hopf method [19], is also found in Ref. [20]. Again, a good agreement is shown between the mode-matching and numerical solutions up to a certain frequency. In addition, Roger et al. [14,16] resorted to the use of Ovenden's solution for the velocity potential [21] to highlight the effect of cut-on/cut-off transition of modes in cambered inter-vane channels, but did not implement this mechanism in the mode-matching procedure. Meanwhile, Mao et al. [22] derived a mode-matching model using a discontinuous representation of a cambered vane in the form of several flat elements. However, the computational efficiency of the model did not seem satisfactory with increasing camber and frequency.

Camber seems to play a significant role in the generation and propagation of sound by stator vanes, but is rarely considered in low-order models. Many authors have noted its importance for tonal noise prediction at moderate and high frequencies [19,23–26], but it does not significantly affect broadband noise [23,27,28]. Accounting for camber has also several benefits in analytical models. When using flat-plate vanes, the choice of an equivalent stagger angle is ambiguous and can have a dramatic impact on noise predictions [29–31]. This is quite understandable when thinking of an equivalent surface distribution of dipoles, as explained by Curle [32]. The complex interference pattern resulting from the radiation of multiple vanes in a cascade is directly influenced by the orientation of the dipoles. Since the unsteady lift generated by the impingement of wakes on the vanes is mainly concentrated near the leading edge, a proper inclination of the leading-edge vane angle should accurately reproduce the upstream radiation, whereas camber should mainly help to recover the downstream pressure field, as noticed by de Laborderie et al. [24]. Finally, flat guide vanes also lead to an ambiguity regarding the mean flow description, which is deviated through the cascade in realistic applications in order to recover the swirl. Hence, the mean flow should vary continuously through the cascade to obtain a relevant sound-propagation framework.

In view of the lack of dedicated literature, a two-dimensional mode-matching model is proposed here to describe the scattering of an acoustic wave by a linear cascade of cambered vanes. Vane thickness is not explicitly considered; furthermore, zero angle of attack is assumed, in the sense that the incident flow is aligned with the vane camber line at leading edge. The modeling is limited to two dimensions, in order to better understand the fundamental effects of camber. Note that the introduction of camber should give rise to the question of mean loading effects on aeroacoustics. Such effects are ignored in the present model. They are addressed, for instance, by Peake and Kerschen [33,34].

The outline of this paper is as follows. First, the mode-matching technique is briefly reminded in Section 2, focusing on the present extension of the model from flat vanes to cambered vanes. An approximate solution of the velocity potential inside the cambered inter-vane channels, needed as the key variable, is derived in Section 3 from the work of Brambley and Peake [35]. Using this potential, the new system of mode-matching equations for cambered vanes is derived in Section 4. The curved-channel modes are analyzed in Section 5 to understand their sensitivity to curvature, Mach number and frequency. Section 6 is dedicated to the validation of the developed mode-matching model by comparing the predicted sound-pressure field with high-fidelity numerical simulations in different conditions, with and without flow. Finally, concluding remarks are drawn in Section 7, alongside perspectives for future work.

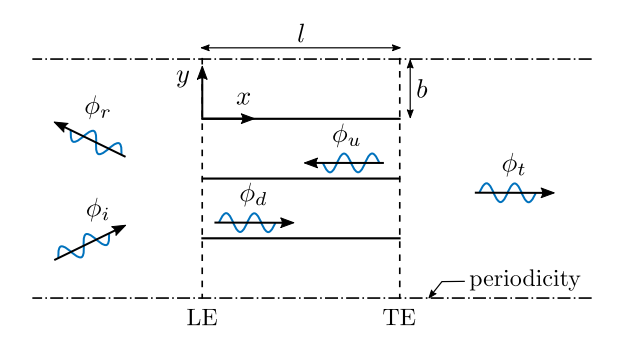


Fig. 1. Scattering of an incident acoustic wave by a linear cascade of flat vanes.

2. Mode-matching technique

2.1. General principles

For a comprehensive description of the method, the reader can refer to, for example, Bouley et al. [6]. Only the general principles are described here in order to highlight the innovative addition of the present paper. The mode-matching technique is well suited when the geometry of the domain, in which the Helmholtz problem must be solved, can be seen as the junction of multiple subdomains. Such problems typically arise as waves propagate inside ducts with successive portions of rigid and lined walls, or as incident waves are scattered when transmitted through bifurcated channels. In particular, sound propagation through a blade row can be viewed as an example of the latter case. When described in a two-dimensional unwrapped cut at a constant radius R, the row is equivalent to an infinite array of bifurcated waveguides. A conceptual sketch is given in Fig. 1. An incident wave, in fact an acoustic mode of the first sub-domain described by its velocity potential ϕ_i , is scattered at the stator Leading-Edge (LE) interface. This generates reflected modes ϕ_r and transmitted modes ϕ_d in the channels. The latter are then scattered at the Trailing-Edge (TE) interface, giving rise to reflected channel modes ϕ_u and transmitted modes ϕ_t . Hard-wall boundary conditions at the walls of the inter-vane channels and periodic boundary conditions in the y-direction are imposed.

The mode-matching technique can be described in three steps: partitioning, modal solving and matching. The partitioning consists in dividing the domain into different sub-domains in which the boundary conditions are uniform, enabling the wave equation in the frequency domain to be solved on a local modal basis. In Fig. 1, the sub-domains are the upstream region, all inter-vane channels and the downstream region. The solving step consists in providing the modal basis and associated wavenumbers of the scattered waves in each sub-domain. For simple geometries such as in Fig. 1, the pairs of eigenfunctions and eigenvalues are determined analytically. Finally, the only remaining unknowns are the coefficients of the modal expansions of the waves. They are defined by matching the different modal solutions at both leading-edge and trailing-edge interfaces. To do so, continuity equations specific to the problem are integrated along the interfaces in order to build an infinite set of equations on the modal coefficients. The equations that need to be satisfied through the stator are derived from the classical continuity equations for mass, momentum and energy. When applied to adiabatic turbomachinery flows, they express the conservation of mass-flow rate and stagnation enthalpy [36]. After modal truncation, the system can be solved numerically. The sub-domains solving step and the matching step are detailed in what follows.

2.2. Solving step: wave equation in the sub-domains

The fluid is assumed to be an inviscid and ideal gas undergoing isentropic transformation. The flow variables are defined as: the velocity \mathbf{u}^* , the density ρ^* , the pressure ρ^* and the sound speed c^* . They are made dimensionless by combinations of the inter-vane spacing b, for length quantities, and the flow field variables far upstream of the cascade: density $D_{-\infty}$ for mass quantities, and sound speed $C_{-\infty}$ for time quantities. The flow is then split into a steady-state component (time average) and its zero-average fluctuations. The fluctuating part varies harmonically in time t, with angular frequency ω , and is assumed to be small enough to allow linearization. Thus, the decomposition reads

$$\left[\mathbf{u}^{*}, \rho^{*}, p^{*}, c^{*}\right] = \left[\mathbf{U}, D, P, C\right] + \left[\mathbf{u}, \rho, p, c\right] e^{-i\omega t},$$
 (1)

where i is the imaginary unit. The velocity potential is related to the fluctuating velocity by

$$\mathbf{u} = \nabla \phi$$
, (2)

and to the fluctuating pressure by

$$p = -D\left(-\mathrm{i}\omega\phi + \mathbf{U}\cdot\nabla\phi\right). \tag{3}$$

The linearized Euler equations and conditions of an isentropic flow of ideal gas lead to the following homogeneous compressible wave equation:

$$D(-i\omega + \mathbf{U} \cdot \nabla) \left[\frac{1}{C^2} (-i\omega + \mathbf{U} \cdot \nabla) \phi \right] - \nabla \cdot (D\nabla \phi) = 0.$$
 (4)

Eq. (4) is solved independently in each subdomain to obtain the local modal basis and wavenumbers.

2.3. Matching step: continuity equations at the interfaces

In the case of an oblique mean flow through the matching interface, typically when stagger or camber is considered, the conservation of mass-flow rate and stagnation enthalpy no longer reduces to the conservation of pressure and axial velocity as in Ref. [6]. Either a Prandtl–Glauert–Lorentz transformation is applied to reduce the problem to its no-flow mathematical equivalent, or more general variables are introduced. The latter choice is made here, in order to avoid unnecessary changes in future works dealing with sound generation by wake impingement.

The first retained conservative variable is (see Appendix A for details)

$$\begin{cases} \Gamma_1 = \phi, & \text{at LE,} \\ \Gamma_1 = p, & \text{at TE.} \end{cases}$$
 (5)

The second conservative variable is a combination of axial u_x and transverse u_y velocities

$$\begin{cases} \Gamma_2 = \beta_x^2 u_x - M_x M_y u_y, & \text{at LE,} \\ \Gamma_2 = u_x, & \text{at TE,} \end{cases}$$
 (6)

where the Mach number components are $M_x = U_x/C$ and $M_y = U_y/C$, and $\beta_x = \sqrt{1 - M_x^2}$. Notice that in the absence of transverse mean flow ($M_y = 0$), the conservation of these new variables at LE is equivalent to the usual conservation of pressure p and axial velocity u_x , of course as long as the mean flow is continuous across the interface.

The conservative variables are gathered into a vector $\Gamma = (\Gamma_1, \Gamma_2)$, for the incident (*i*), reflected annular (*r*), transmitted annular (*t*), downstream-propagating channel (*d*) or upstream-propagating channel (*u*) field (see Fig. 1). The matching equations then read

$$\begin{cases} \Gamma_i + \Gamma_r = \Gamma_d + \Gamma_u, & \text{at LE,} \\ \Gamma_d + \Gamma_u = \Gamma_t, & \text{at TE.} \end{cases}$$
 (7)

Only the knowledge of the potential field ϕ , and its gradient, is required to solve the matching equations in this case. Upstream and downstream of the cascade, its description is already known from Bouley et al. [6]. Therefore, the innovative contribution of this article consists in the addition of the velocity potential in the cambered inter-vane channels from Eq. (4).

3. Velocity potential in a cambered inter-vane channel

3.1. Geometry

3.1.1. Circle arc

The cambered vanes are modeled by circle arcs, which means that a constant curvature distribution along the chord is assumed; the associated curvature radius is noted R_c . Fig. 2 shows how the stagger angle Ψ_s , the camber angle Ψ and the axial chord length I_x are introduced. Ψ is the angle formed by the tangents to the vane leading and trailing edges. Since the stator trailing edge is aligned with the x-axis, i.e. the turbomachinery axis, the camber angle Ψ is equivalent to the leading-edge vane angle. Furthermore, because the vanes are circle arcs, $\Psi_s = \Psi/2$ and thus $I_x = I\cos\Psi/2$. The addition of camber has a twofold impact on sound propagation through the inter-vane channels. Indeed, the channel is curved, but its cross-section also expands from the inlet (leading edge) to the outlet (trailing edge).

3.1.2. Geometrical approximation

The need to cope with the vane overlap leads to split the inter-vane channel into two parts delimited by the segment BC in Fig. 3(a): a semi-open part delimited by the triangle ABC, and a curved channel of varying cross-section from the section BC to the trailing-edge interface, as represented in Fig. 3(b) with its curvilinear coordinates (s, n, z).

Instead of following the exact camber line defined as a circle arc in Fig. 2, the choice is made to modify the suction side to facilitate mathematical tractability in subsequent derivations. Segment AC in Fig. 3(a) follows the tangent to the vane leading-edge, hence the triangle ABC is the same as for straight staggered plates already studied for electromagnetic and acoustic waves as will be discussed in Section 3.1.3. With this choice, the geometric difference induced by curvature only concerns the overlapping part from interface BC to the trailing edge interface. Different possibilities remain to define the curve from point C to the trailing edge, on the suction side of the vane. To ensure zero tangent at the trailing edge, thus avoiding another triangular part on this side, the following parametric representation is used:

$$\begin{cases} x_{ss}(\varphi) = R_c \left(\sin \varphi + \sin \Psi \right) - b \cos \varphi \sin \varphi, \\ y_{ss}(\varphi) = R_c \left(\cos \varphi - \cos \Psi \right) + b \sin^2 \varphi, \end{cases}$$
 (8)

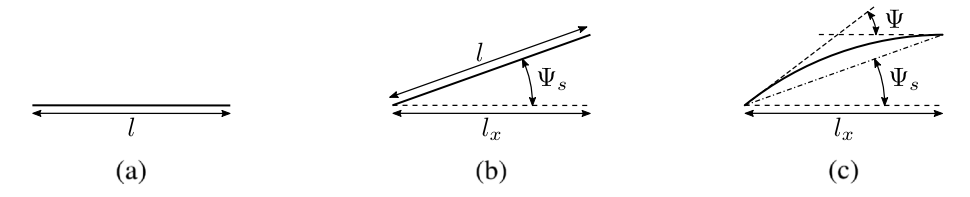


Fig. 2. Description of the vanes from flat and axial (a) to staggered (b) and curved and staggered (c).

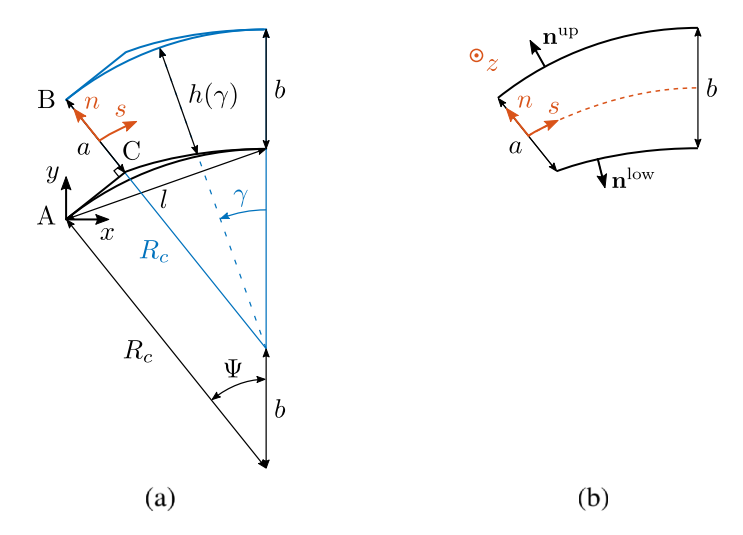


Fig. 3. Geometrical approximation of the inter-vane channel (a) and the curved channel of varying cross-section from section BC to the trailing-edge interface (b).

where $\varphi = -\Psi$ at the inlet and $\varphi = 0$ at the outlet (see Fig. 3(a)). Since a zero tangent is enforced at the trailing edge, non-monotonic curves can arise for high camber angles, depending on the solidity value l/b. This might be considered unrealistic. The limit at which it occurs is given by $\Psi \geq \Psi_c = 2 \arcsin(l/4b)$. This corresponds to 44° for l/b = 1.5, which is outside the range of camber angles used for turbofan outlet guide vanes. In addition, the continuity of the derivative is not enforced at point C, resulting in an angular point. Smoothing out the transition would be detrimental to the critical camber angle Ψ_c . It will be shown that this angular point is not a concern for sound prediction by comparisons with numerical results in Section 6.2.2.

The upper-vane pressure side is a circle arc described by

$$\begin{cases} x_{ps}(\varphi) = R_c \left(\sin \varphi + \sin \Psi \right), \\ y_{ps}(\varphi) = R_c \left(\cos \varphi - \cos \Psi \right) + b. \end{cases}$$
 (9)

The channel center line is represented by a dashed red line in Fig. 3(b); the parametric representation of which is given by

$$\begin{cases} x_s(\varphi) = R_c \left(\sin \varphi + \sin \Psi \right) - \frac{b}{2} \cos \varphi \sin \varphi, \\ y_s(\varphi) = R_c \left(\cos \varphi - \cos \Psi \right) + \frac{b}{2} \left(1 + \sin^2 \varphi \right), \end{cases}$$
 (10)

and the associated curvilinear abscissa s by

$$s = \int_{-\Psi}^{\varphi} \sqrt{\left(\frac{\mathrm{d}x_s}{\mathrm{d}\varphi'}\right)^2 + \left(\frac{\mathrm{d}y_s}{\mathrm{d}\varphi'}\right)^2} \,\mathrm{d}\varphi' \underset{b/R_c \to 0}{\sim} R_c(\varphi + \Psi), \quad -\Psi \le \varphi \le 0. \tag{11}$$

The channel length $s(\varphi = 0)$ is noted l_c in the following. From Eqs. (8) and (9), the varying channel height is given by

$$h(\varphi) = \sqrt{(x_{ps} - x_{ss})^2 + (y_{ps} - y_{ss})^2} = b\cos\varphi \sum_{b/R_c \to 0} b\cos(s/R_c - \Psi), \quad 0 \le s \le l_c.$$
 (12)

The approximate inlet height $a = b \cos \Psi$ of segment BC (Fig. 3(a)) is smaller than the original height \bar{a} between two circle arcs by an amount

$$\frac{\bar{a} - a}{R_c} = 1 - \sqrt{1 - \left(\frac{b}{l} \frac{\sin^2 \Psi}{\cos \Psi/2}\right)^2}.$$
 (13)

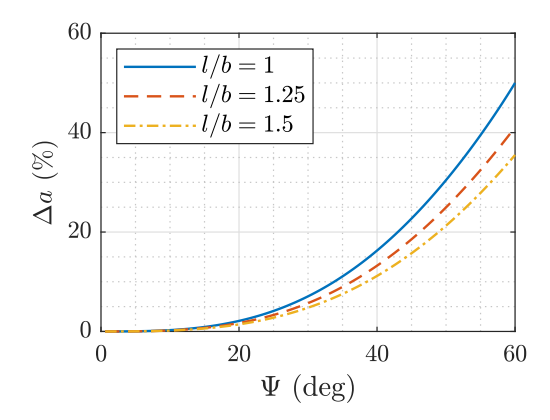


Fig. 4. Evolution of the inlet height relative deviation $\Delta a = (\bar{a} - a)/\bar{a}$ against the camber angle Ψ for different solidity values l/b.

This deviation being only dependent on the camber angle Ψ and the solidity l/b, its relative value $\Delta a = (\bar{a} - a)/\bar{a}$ is plotted in Fig. 4. It is negligible (less than 2%) for camber angles below 20°, but can reach 10% at $\Psi = 36^\circ$. In this case, the approximation tends to significantly increase the height expansion of the inter-vane channel compared to the mean camber line. Yet, this artificial thickness, albeit arbitrary because dictated by the need for mathematical tractability, is also a way to mimic the actual thickness of real vanes. For this reason, the mathematical process is believed relevant. Whether or not this artificial thickness helps in the prediction of sound propagation with a realistic vane profile is investigated in Section 6.2.2.

3.1.3. Modal basis approximation in the triangle ABC

Whitehead [2] proposed to use Green's second identity to link the pressure field from the leading-edge interface to the segment BC in the channel, by taking advantage of the absence of acoustic sources inside the triangle ABC (Fig. 3(a)). The identity was used by Roger and François [16] and could be coupled with Kirchhoff's integral theorem to give access to the pressure field inside the triangle. A convenient formulation has also been proposed by Roger et al. [14] who described the pressure field in this part as if it were a channel of height a and length $b \sin \Psi$. In this case, cosine functions are used as a modal basis and the matching at the leading-edge interface is done classically, by considering a staggered interface for the channel modes. A good agreement between both formulations was reported in Ref. [14]. Consequently, the approximate modal basis is used in the present study for its simplicity.

3.1.4. Multiple-scale approximation from section BC to the trailing edge

In the varying part of the channel, one last approximation is needed. If the cross-section varies slowly along the channel, the method of multiple scales can be used to derive a closed-form solution of the velocity potential. The idea behind the method of multiple scales is that the variation of cross-section occurs on a much larger scale than the acoustic motion and is defined by a new and independent coordinate $S = \epsilon s$, where ϵ is a small parameter. Each field is then expressed as a regular asymptotic expansion in powers of ϵ and an approximate solution is found at leading order, accounting for both fast and slow variations. This formalism has been used by many authors in turbomachinery acoustics [37–44], and proved its efficiency against numerical results [45,46]. In the present case, ϵ corresponds to the maximal value of the cross-section derivative, i.e. the local slope of the channel walls, and is assumed small enough in the following. From Eq. (12), it can be estimated by

$$\epsilon \underset{b/R_c \to 0}{\sim} \frac{b}{R_c} \sin \Psi = \frac{b}{l} \frac{\sin^2 \Psi}{\cos \Psi/2}.$$
 (14)

Note the link between this assumption and the artificial thickness in Eq. (13), which becomes $\mathcal{O}(\epsilon^2)$.

3.2. Mean flow

The incident mean flow is considered uniform and perfectly aligned with the vane leading edges. It is described by

$$\mathbf{U}_{-\infty}(x,y) = U_{-\infty}\cos\Psi \,\mathbf{e}_x + U_{-\infty}\sin\Psi \,\mathbf{e}_y, \quad -\infty < x \le 0 \quad \text{and} \quad 0 \le y < 2\pi R, \tag{15}$$

where the $-\infty$ subscript denotes the fields upstream of the stator.

Beyond the leading-edge interface (x > 0), the mean-flow velocity remains constant in the triangle ABC; then the flow enters the slowly varying part. Here, the mean velocity is assumed to be uniform in every cross-section normal to the curvilinear coordinate S, hence only varying with S. The mean flow variables are expanded as

$$U(S,n) = U_{0,\epsilon}(S)e_s + \epsilon U_{1,n}(S,n)e_n + \mathcal{O}(\epsilon^2), \tag{16a}$$

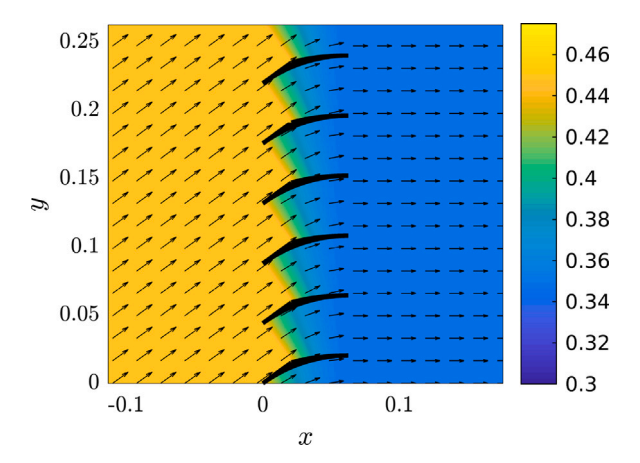


Fig. 5. Modeled total Mach number and flow angle evolution through a cascade of cambered vanes, according to the present vane model. Geometry and flow conditions from Ref. [47].

$$D(S, n) = D_0(S) + \mathcal{O}(\epsilon^2), \tag{16b}$$

$$C(S, n) = C_0(S) + \mathcal{O}(\varepsilon^2). \tag{16c}$$

The value of $U_{0s}(S)$ is given by the conservation of mass-flow rate between a given location S and the inlet (interface BC). This gives

$$U_{0s}(S) = U_{-\infty} \frac{D_{-\infty} a}{D_0(S)h(S)}, \quad 0 \le S \le L_c,$$
(17)

where $L_c = \epsilon l_c$ is the channel length expressed in the slow variable. If the compressibility effects are accounted for, the evolution of the mean density $D_0(S)$ has to be computed first using the momentum equation. Neglecting the rotational term at leading order leads to Bernoulli's equation, which gives the density as one of the roots of the following polynomial function

$$D_0(S) \mapsto \frac{1}{\gamma - 1} D_0^{\gamma + 1}(S) - \left(\frac{U_{-\infty}^2}{2} + \frac{D_{-\infty}^{\gamma - 1}}{\gamma - 1}\right) D_0^2(S) + \frac{1}{2} \left(\frac{D_{-\infty} U_{-\infty} a}{h(S)}\right)^2, \tag{18}$$

where γ is the ratio of specific heats. The value of $D_0(S)$ is found by applying Newton–Raphson method at each location S, with an initial guess equal to $D_{-\infty}$ in order to converge to the desired root. The speed of sound is then solely determined by the density, in dimensionless form, as

$$C_0(S) = \sqrt{D_0^{\gamma - 1}(S)}. (19)$$

Downstream of the stator, the mean flow exits the channels without deviation. It is defined as

$$\mathbf{U}_{+\infty}(x,y) = U_{-\infty} \cos \Psi \frac{D_{-\infty}}{D_{+\infty}} \mathbf{e}_x, \quad l_x \le x < \infty \quad \text{and} \quad 0 \le y < 2\pi R,$$
 (20)

where the $+\infty$ subscript denotes the fields downstream of the stator. The evolution of the mean flow field through the cascade is displayed in Fig. 5.

3.3. Slowly varying acoustic modes

3.3.1. Problem formulation

In the slowly varying part of the inter-vane channels (Fig. 3(b)), the compressible wave Eq. (4) can be recast in terms of powers of ϵ using the mean flow description from Eq.(16). Introducing the scale factor for the curvilinear coordinate s as

$$h_s = 1 + n/R_c, -h(S)/2 \le n \le h(S)/2,$$
 (21)

the wave Eq. (4) reads

$$\epsilon^{2} \frac{\beta^{2}}{h_{s}^{2}} \frac{\partial^{2} \phi}{\partial S^{2}} + \frac{\partial^{2} \phi}{\partial n^{2}} + 2i\epsilon \frac{kM}{h_{s}} \frac{\partial \phi}{\partial S} + \frac{1}{h_{s} R_{c}} \frac{\partial \phi}{\partial n} + k^{2} \phi = \mathcal{O}(\epsilon), \tag{22}$$

where $M = U_{0s}/C_0$, $\beta = \sqrt{1 - M^2}$ and $k = \omega/C_0$. The hard wall boundary conditions are written as

$$(\nabla \phi \cdot \mathbf{n}) = 0$$
, at $n = \pm h(S)/2$, (23)

where \mathbf{n} is the outer normal unit vector to the respective wall, slightly misaligned with \mathbf{e}_n due to height expansion (Fig. 3(b)). The normal vectors to the upper and lower boundaries are written respectively

$$\mathbf{n}^{\text{up}} = \frac{\mathbf{e}_n - \frac{\epsilon}{h_s} \frac{dh}{dS} \mathbf{e}_s}{\sqrt{1 + \frac{\epsilon^2}{h_s^2} \left(\frac{dh}{dS}\right)^2}}, \quad \mathbf{n}^{\text{low}} = -\frac{\mathbf{e}_n + \frac{\epsilon}{h_s} \frac{dh}{dS} \mathbf{e}_s}{\sqrt{1 + \frac{\epsilon^2}{h_s^2} \left(\frac{dh}{dS}\right)^2}}, \quad \text{at} \quad n = \pm h(S)/2.$$
(24)

A well suited technique for finding an approximate solution of Eq. (22) is the WKB method. The WKB approximation is a special case of multiple-scale analysis in which the fast variations (dependence on *s*) are assumed to be of exponential form (see for example Ref. [48] or [49]). The asymptotic series expansion of the slowly-varying potential reads

$$\phi(S,n) = \exp\left(\frac{\mathrm{i}}{\epsilon} \int_{-\infty}^{S} \mu(\xi) \,\mathrm{d}\xi\right) \sum_{m=0}^{\infty} \epsilon^m \Phi_m(S,n),\tag{25}$$

where $\mu(S)$ is the acoustic wavenumber along the curvilinear abscissa that is now able to vary with S. Introducing the above expansion into the wave Eq. (22) yields, at leading order,

$$\frac{\partial^2 \boldsymbol{\Phi}_0}{\partial n^2} + \frac{1}{h_s R_c} \frac{\partial \boldsymbol{\Phi}_0}{\partial n} + \left(\left[k - \frac{\mu}{h_s} M \right]^2 - \frac{\mu^2}{h_s^2} \right) \boldsymbol{\Phi}_0 = 0. \tag{26}$$

Since the misalignment of the normal unit vectors with \mathbf{e}_n is $\mathcal{O}(\epsilon)$ by definition in Eq. (24), the upper and lower boundaries can be assumed parallel at leading order. The boundary conditions, Eq. (23), yield

$$\left. \frac{\partial \Phi_0}{\partial n} \right|_{n=\pm h(S)/2} = 0. \tag{27}$$

Finally, the leading-order solution Φ_0 is split up into its amplitude N and mode shape ψ , with the following normalization

$$\Phi_0(S, n) = N(S)\psi(S, n), \quad \int_{-h(S)/2}^{h(S)/2} \psi^2(S, n) \, \mathrm{d}n = 1.$$
 (28)

3.3.2. Mode shape and axial wavenumber

When M=0, the mode-shape Eq. (26) can be restated as a Bessel equation by a change of variable $r=n+R_c$ and introducing $v=\mu R_c$. The solution for a single mode is expressed by a sum of Bessel functions of the first and second kinds, J_{ν} and Y_{ν} respectively, such that

$$\psi(S,r) = C_1 J_{ij}(kr) + C_2 Y_{ij}(kr), \quad v \in \mathbb{C}, \quad 0 \le r < \infty.$$

$$\tag{29}$$

The dimensionless axial wavenumber ν and the ratio C_1/C_2 are defined at each location S by the algebraic equations resulting from the hard-wall boundary conditions at leading order, Eq. (27). The latter read

$$-\frac{C_1}{C_2} = \frac{\partial Y_{\nu}/\partial r \left(k \left[R_c + h(S)/2\right]\right)}{\partial J_{\nu}/\partial r \left(k \left[R_c + h(S)/2\right]\right)} = \frac{\partial Y_{\nu}/\partial r \left(k \left[R_c - h(S)/2\right]\right)}{\partial J_{\nu}/\partial r \left(k \left[R_c - h(S)/2\right]\right)}.$$
(30)

The choice is made to take

$$C_1 = \frac{\partial Y_{\nu}}{\partial r} \left(k \left[R_c + h(S)/2 \right] \right), \quad \text{and} \quad C_2 = -\frac{\partial J_{\nu}}{\partial r} \left(k \left[R_c + h(S)/2 \right] \right), \tag{31}$$

to enforce the boundary condition on the upper part (n = +h(S)/2). Hence v(S) is defined by the boundary condition on the lower part (n = -h(S)/2) as

$$\frac{\partial Y_{\nu}}{\partial r} \left(k \left[R_c + h(S)/2 \right] \right) \frac{\partial J_{\nu}}{\partial r} \left(k \left[R_c - h(S)/2 \right] \right) - \frac{\partial J_{\nu}}{\partial r} \left(k \left[R_c + h(S)/2 \right] \right) \frac{\partial Y_{\nu}}{\partial r} \left(k \left[R_c - h(S)/2 \right] \right) = 0, \tag{32}$$

which describes implicitly the dispersion relation between k and $\mu = v/R_c$. Now written in terms of n instead of r, the mode shapes of Eq. (29) read

$$\psi(S,n) \propto \frac{\partial Y_{\nu}}{\partial n} \left(k \left[R_c + h(S)/2 \right] \right) J_{\nu}(k[n+R_c]) - \frac{\partial J_{\nu}}{\partial n} \left(k \left[R_c + h(S)/2 \right] \right) Y_{\nu}(k[n+R_c]). \tag{33}$$

The proportionality factor is determined by the normalization Eq. (28). This two-dimensional solution is actually an extension of Krasnushkin's result [50] to slowly varying ducts.

In the present framework of analysis for arbitrary subsonic flows, 0 < M < 1, Eq. (26) no longer reduces to a linear eigenvalue problem. In this work, the choice is made to develop a numerical solution using the same procedure as in Refs. [8,35]. A pseudospectral method based on Chebyshev polynomials of the first kind is used, the details of which can be found in Appendix B. Introducing $\psi^* = \mu \psi$ makes the eigenvalue problem linear in terms of the vector (ψ, ψ^*) . The generalized eigenvalue problem to be solved is then

$$\begin{bmatrix} \mathcal{L} & 0 \\ 0 & 1 \end{bmatrix} \begin{bmatrix} \psi \\ \psi^* \end{bmatrix} = \mu \begin{bmatrix} 2kM/h_s & \beta^2/h_s^2 \\ 1 & 0 \end{bmatrix} \begin{bmatrix} \psi \\ \psi^* \end{bmatrix}, \tag{34}$$

where

$$\mathcal{L} := \frac{\partial^2}{\partial n^2} + \frac{1}{h_* R_n} \frac{\partial}{\partial n} + k^2. \tag{35}$$

The validity of the numerically solved modal basis ψ and wavenumbers μ is assessed by comparing asymptotic behaviors to analytical solutions in Section 5.

3.3.3. Amplitude evolution

For a given mode, the unknown amplitude N(S) from Eq. (28) is determined by means of a solvability condition. From Brambley and Peake [35], an adiabatic invariant exists at leading order in the form of

$$\frac{\mathrm{d}}{\mathrm{d}\mathbf{S}}\left(FN^{2}\right) = \mathcal{O}(\epsilon),\tag{36}$$

where F(S) is defined by

$$F(S) = \int_{-h(S)/2}^{h(S)/2} D_0 \psi^2 \left(kM h_s + \beta^2 \mu \right) \frac{\mathrm{d}n}{h_s}.$$
 (37)

This leads to the solution

$$N^{2}(S) = \frac{Q^{2}}{F(S)},\tag{38}$$

where Q is a constant to be determined by a known value of N(S) (typically at the inlet). In the end, the approximate velocity potential of a given mode in a slowly varying inter-vane channel is given by

$$\phi(S,n) \sim \frac{Q}{\sqrt{F(S)}} \psi(S,n) \exp\left(\frac{\mathrm{i}}{\epsilon} \int_{-\infty}^{S} \mu(\xi) \,\mathrm{d}\xi\right). \tag{39}$$

The matching equations, as presented in Ref. [51], are detailed in the next section.

4. System of mode-matching equations

4.1. Leading-edge interface

4.1.1. Definition of the acoustic potentials

The description of the leading-edge matching, including all the potentials involved, is sketched in Fig. 6. The incident acoustic wave is described as a mode of unitary amplitude and azimuthal order j, with transverse wavenumber α_j and axial wavenumber k_j , such as

$$\phi_i(x, y) = e^{i\alpha_j y} e^{ik_j^+ x}, \quad -\infty < x \le 0, \quad 0 \le y < 2\pi R.$$
(40)

The transverse wavenumber α_j is given by enforcing the periodicity $\phi_i(x,0) = \phi_i(x,2\pi R)$, whereas the axial wavenumber k_j is given by solving the Helmholtz Eq. (4) with a transverse mean flow and a solution of the form of Eq. (40). This gives

$$\alpha_j = \frac{j}{R}, \quad k_j^+ = -\frac{(k-\alpha_j M_y) M_x}{\beta_x^2} + \frac{\sqrt{(k-\alpha_j M_y)^2 - \beta_x^2 \alpha_j^2}}{\beta_x^2}, \quad j \in \mathbb{Z}.$$

The axial wavenumber with a transverse mean flow has the same structure than with an axial mean flow [6], but with a modified effective frequency $k \to k - \alpha_j M_y$ due to the mean flow component M_y , which increases/decreases the wavelength of the modes propagating in the same/opposite direction, respectively.

To comply with the periodicity of the cascade, the reflected potential ϕ_r is expressed as a sum of scattered modes of complex amplitudes R_n as (see Ref. [6])

$$\phi_r(x, y) = \sum_{p = -\infty}^{\infty} R_p e^{i\alpha_p y} e^{ik_p^{-x}}, \quad -\infty < x \le 0, \quad 0 \le y < 2\pi R,$$
(41)

where the wavenumbers are

$$\alpha_p = \alpha_j + p \frac{2\pi}{b}, \quad k_p^{\pm} = -\frac{(k - \alpha_p M_y) M_x}{\beta_x^2} \pm \frac{\sqrt{(k - \alpha_p M_y)^2 - \beta_x^2 \alpha_p^2}}{\beta_x^2}, \quad p \in \mathbb{Z}.$$

Here, the transverse wavenumber α_p is enforced by the trace-velocity matching principle [52], which is a consequence of causality under steady-state circumstances.

In the triangle ABC, the channel modes of potentials ϕ_d and ϕ_u are written in terms of the coordinate system attached to the vanes (ζ, η) defined in Fig. 6. With complex amplitudes A_q and \tilde{B}_q , respectively, and considering hard-wall boundary conditions, they read

$$\phi_d(\zeta, \eta) = \sum_{q=0}^{\infty} A_q \cos\left(\alpha_q \eta\right) e^{ik_q^+ \zeta}, \quad \eta \tan \Psi \le \zeta \le a \tan \Psi, \quad 0 \le \eta \le a, \tag{42}$$

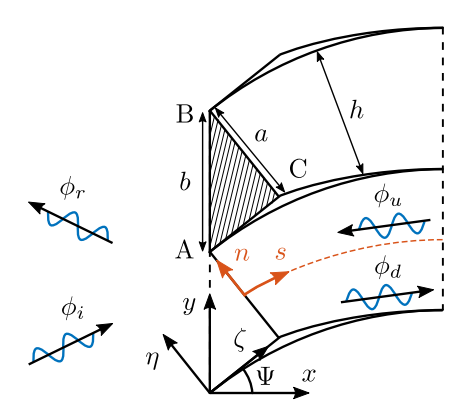


Fig. 6. Scattering of an incident mode at the staggered leading-edge interface with feedback from the trailing-edge scattering.

$$\phi_{u}(\zeta,\eta) = \sum_{q=0}^{\infty} \tilde{B}_{q} \cos\left(\alpha_{q} \eta\right) e^{\mathrm{i}k_{q}^{-}(\zeta - a \tan \Psi)}, \quad \eta \tan \Psi \leq \zeta \leq a \tan \Psi, \quad 0 \leq \eta \leq a, \tag{43}$$

where the associated wavenumbers are given by

$$\alpha_q = \frac{q\pi}{a}, \quad k_q^\pm = -\frac{kM}{\beta^2} \pm \frac{\sqrt{k^2 - \beta^2 \alpha_q^2}}{\beta^2}, \quad q \in \mathbb{N}.$$

In Eq. (43), the origin of the upstream-propagating channel modes is considered at the interface BC, but in fact their origin is the trailing-edge interface. This requires to modify the complex amplitude \tilde{B}_q to account for the effects of curvature during the propagation from the trailing edge to the interface BC. In order to compare the channel modal coefficients with and without accounting for curvature, they are always associated to cosine modes at the origin. Hence, a cosine mode $\phi_{u,q}$ is first expanded in curved-channel modes ψ_l at the trailing-edge interface, such that

$$\phi_{u,q}(L_c,n) = B_q \sum_{l=0}^{\infty} \mathcal{B}_l^q(L_c) \psi_l(L_c,n),$$

where B_q is the complex coefficient of the cosine mode. The projection coefficients $\mathcal{B}_l^q(S)$ of a cosine mode indexed q onto curved-channel modes indexed l are defined by

$$\cos\left(\frac{q\pi}{h(S)}\left[n+\frac{h(S)}{2}\right]\right) = \sum_{l=0}^{\infty} \mathcal{B}_l^q(S)\psi_l(S,n), \quad 0 \le S \le L_c, \quad -\frac{h(S)}{2} \le n \le \frac{h(S)}{2}. \tag{44}$$

The amplitude and phase evolution of each of these curved-channel modes, from the trailing-edge interface to the interface BC, is given by the stream-wise variation function Y_i^- :

$$Y_l^-(S) = \sqrt{\frac{F_l^-(L_c)}{F_l^-(S)}} \exp\left(\frac{\mathrm{i}}{\epsilon} \int_{L_c}^S \mu_l^-(\xi) \,\mathrm{d}\xi\right), \quad 0 \le S \le L_c, \tag{45}$$

where F_l^- is identical to the function F defined in Eq. (37) for the upstream-propagating mode of order l and axial wavenumber μ_l^- . Finally, each of the curved-channel modes has to be expanded back to cosine modes indexed q^* at the interface BC, which yields

$$\phi_{u,q}(0,n) = B_q \sum_{l=0}^{\infty} B_l^q(L_c) Y_l^-(0) \sum_{*=0}^{\infty} A_{q^*}^l(0) \cos\left(\alpha_{q^*} \left[n + \frac{a}{2}\right]\right), \tag{46}$$

where the coefficients $\mathcal{A}_{a^*}^l(S)$ result from the inverse projection

$$\psi_{l}(S, n) = \sum_{q^{*}=0}^{\infty} \mathcal{A}_{q^{*}}^{l}(S) \cos \left(\frac{q\pi}{h(S)} \left[n + \frac{h(S)}{2} \right] \right), \quad 0 \le S \le L_{c}, \quad -\frac{h(S)}{2} \le n \le \frac{h(S)}{2}. \tag{47}$$

The complex coefficients \tilde{B}_q in the triangle ABC can now be expressed in terms of the B_q by equating both formulations in Eqs. (43) and (46). This ensures the continuity of the potential at the interface BC. Notice that the geometrical approximation of the inter-vane channel is in two parts: a straight channel in the triangle ABC, and a curved channel from interface BC to the trailing edge. This introduces an artificial curvature discontinuity at the junction, interface BC, that should generate scattering and reflection. This is neglected in the present model because it is a spurious effect of the approximation, not physically consistent. The reflection should be negligible anyway, because of the relatively low dimensionless curvature and angular length of the inter-vane channels compared

to those of the bent ducts studied in, for example, Ref. [53]. In the end, the potential ϕ_{μ} is expressed in the triangle ABC as

$$\phi_{u}(\zeta,\eta) = \sum_{q=0}^{\infty} B_{q} \sum_{l=0}^{\infty} \beta_{l}^{q}(L_{c}) Y_{l}^{-}(0) \sum_{q^{*}=0}^{\infty} \mathcal{A}_{q^{*}}^{l}(0) \cos\left(\alpha_{q^{*}}\eta\right) e^{ik_{q^{*}}^{-}(\zeta - a\tan\Psi)}. \tag{48}$$

4.1.2. Matching equations

The leading-edge matching equation written $\Gamma_d + \Gamma_u = \Gamma_r + \Gamma_i$ involves infinite sums. They need to be expanded into either the unwrapped-annular or channel modal basis in order to obtain a linear system of equations by virtue of the orthogonality of the modes. Using the projection on the annular modal basis

$$\int_{0}^{b} (\bullet) e^{-i\alpha_{p} y} dy, \quad \text{with} \quad \alpha_{p} = \alpha_{j} + p \frac{2\pi}{b}, \ p \in \mathbb{Z}, \tag{49}$$

leads to the continuity of the potential and of the modified acoustic velocity $(\beta_x^2 u_x - M_x M_y u_y)$, respectively, as (see Appendix C for details)

$$\sum_{q=0}^{\infty} \left[A_q \mathcal{I}_{q,p}^+ + B_q \sum_{l=0}^{\infty} \mathcal{B}_l^q(L_c) Y_l^-(0) \sum_{q^*=0}^{\infty} \mathcal{A}_{q^*}^l(0) e^{-ik_{q^*}^- b \sin \Psi} \mathcal{I}_{q^*,p}^- \right] = b \left(R_p + \delta_{p,0} \right), \tag{50}$$

$$\sum_{q=0}^{\infty} \left[A_q \mathcal{K}_{q,p}^+ \mathcal{I}_{q,p}^+ + B_q \sum_{l=0}^{\infty} B_l^q (L_c) Y_l^-(0) \sum_{q^*=0}^{\infty} \mathcal{A}_{q^*}^l(0) e^{-ik_{q^*}^- b \sin \Psi} \mathcal{K}_{q^*,p}^- \mathcal{I}_{q^*,p}^- \right] = b \left(\mathcal{K}_p^- R_p + \mathcal{K}_j^+ \delta_{p,0} \right), \tag{51}$$

where δ is the Kronecker delta.

$$\mathfrak{I}_{q,p}^{\pm}(\Psi) = \begin{cases}
\frac{-\mathrm{i}(k_q^{\pm}\sin\Psi - \alpha_p)}{(q\pi/b)^2 - (k_q^{\pm}\sin\Psi - \alpha_p)^2} \left(1 - (-1)^q \mathrm{e}^{\mathrm{i}b(k_q^{\pm}\sin\Psi - \alpha_p)}\right), \\
\frac{b}{2} \left(1 + \delta_{q,0}\right) & \text{if } \left|k_q^{\pm}\sin\Psi - \alpha_p\right| = \frac{q\pi}{b},
\end{cases}$$
(52)

and the staggered axial wavenumbers are defined by

$$\mathcal{K}_i^+ = \beta_x^2 k_i^+ - M_x M_y \alpha_j,$$

$$\mathcal{K}_p^- = \beta_x^2 k_p^- - M_x M_y \alpha_p,$$

$$\mathcal{K}_{q,p}^{\pm} = \left(\beta_x^2 \cos \Psi - M_x M_y \sin \Psi\right) k_q^{\pm} + \frac{\tan \Psi}{k_q^{\pm} \sin \Psi - \alpha_p} \left(\frac{q\pi}{b}\right)^2.$$

These wavenumbers are said 'staggered' because they tend to the actual axial wavenumbers k^{\pm} when $\Psi \to 0$, so the matching equation on axial velocity for flat-plate vanes [6] is retrieved.

4.2. Trailing-edge interface

4.2.1. Definition of the acoustic potentials

The trailing-edge matching involves the curved-channel potentials ϕ_d and ϕ_u , which need to be matched with the transmitted potential ϕ_t as represented in Fig. 7. A new coordinate system attached to the trailing edge (x', y') is defined for that purpose. The coefficients B_q of the upstream-propagating modes $\phi_{u,q}$ have been associated to cosine modes generated at the trailing-edge interface. Hence, the related potential is given by

$$\phi_u(L_c, y') = \sum_{q=0}^{\infty} B_q \cos\left(\frac{q\pi}{b}y'\right).$$

Following the same procedure for the downstream-propagating modes $\phi_{d,q}$, the coefficients A_q are associated to cosine modes generated at the leading-edge interface. After an expansion on the curved-channel modes at the interface BC, and introducing the stream-wise variation function Y_i^+ as

$$Y_l^+(S) = \sqrt{\frac{F_l^+(0)}{F_l^+(S)}} \exp\left(\frac{\mathrm{i}}{\epsilon} \int_0^S \mu_l^+(\xi) \,\mathrm{d}\xi\right), \quad 0 \le S \le L_c, \tag{53}$$

where F_i^+ is defined by Eq. (37), the related potential reads

$$\phi_d(L_c,y') = \sum_{a=0}^\infty A_q e^{\mathrm{i}k_q^+ a \tan \Psi} \sum_{l=0}^\infty \mathcal{B}_l^q(0) Y_l^+(L_c) \sum_{a^*=0}^\infty \mathcal{A}_{q^*}^l(L_c) \cos \left(\frac{q^*\pi}{b}y'\right).$$

The transmitted potential ϕ_t and its wavenumbers are expressed in the same manner as ϕ_r from Eq. (41) (see Ref. [6]). Thus

$$\phi_t(x', y') = \sum_{p = -\infty}^{\infty} T_p e^{i\alpha_p y'} e^{ik_p^+ x'}, \quad 0 \le x' < \infty, \quad 0 \le y' < 2\pi R.$$

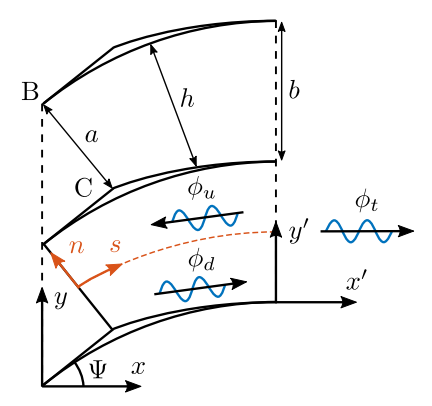


Fig. 7. Scattering of a downstream-propagating channel mode at the trailing-edge interface.

4.2.2. Matching equations

The matching equation is written $\Gamma_d + \Gamma_u = \Gamma_t$. Projecting on the annular modal basis, as in Eq. (49), leads to the potential continuity

$$\sum_{q=0}^{\infty} \left[A_q e^{ik_q^+ b \sin \Psi} \sum_{l=0}^{\infty} B_l^q(0) Y_l^+(L_c) \sum_{q^*=0}^{\infty} \mathcal{A}_{q^*}^l(L_c) \mathfrak{I}_{q^*,p}^0 + B_q \mathfrak{I}_{q,p}^0 \right] = b T_p, \tag{54}$$

where

$$\mathfrak{I}_{q,p}^{0}=\mathfrak{I}_{q,p}^{\pm}(\varPsi=0).$$

The leading-order variation of the potentials along the channel is given by the exponential term in Y^{\pm} from Eqs. (45) and (53). The axial velocity of the curved-channel modes is then defined by

$$\epsilon \frac{\partial \phi_u}{\partial S}(S,n) = \mathrm{i} \sum_{q=0}^\infty B_q \sum_{l=0}^\infty B_l^q(L_c) \frac{\mu_l^-(S)}{h_s} Y_l^-(S) \psi_l(S,n) + \mathcal{O}(\epsilon),$$

and

$$\epsilon \frac{\partial \phi_d}{\partial S}(S,n) = \mathrm{i} \sum_{q=0}^\infty A_q \mathrm{e}^{\mathrm{i} k_q^+ b \sin \Psi} \sum_{l=0}^\infty \mathcal{B}_l^q(0) \frac{\mu_l^+(S)}{h_s} Y_l^+(S) \psi_l(S,n) + \mathcal{O}(\epsilon).$$

As a consequence, a new projection is needed to expand the functions $\psi_l(S,n)/h_s(n)$ into cosine functions. It reads

$$\frac{\psi_l(S, n)}{1 + n/R_c} = \sum_{q^*=0}^{\infty} \tilde{\mathcal{A}}_{q^*}^l(S) \cos\left(\frac{q^*\pi}{h(S)} \left[n + \frac{h(S)}{2}\right]\right), \quad 0 \le S \le L_c, \quad -\frac{h(S)}{2} \le n \le \frac{h(S)}{2}. \tag{55}$$

Finally, the continuity of axial velocity at the trailing-edge interface reads

$$\sum_{q=0}^{\infty} \sum_{l=0}^{\infty} \sum_{q^*=0}^{\infty} \left[A_q e^{ik_q^+ b \sin \Psi} \mathcal{B}_l^q(0) \mu_l^+(L_c) Y_l^+(L_c) + B_q \mathcal{B}_l^q(L_c) \mu_l^-(L_c) \right] \tilde{\mathcal{A}}_{q^*}^l(L_c) \mathfrak{I}_{q^*,p}^0 = b k_p^+ T_p.$$
 (56)

All four Eqs. (50), (51), (54) and (56) are then gathered to yield the linear system to be solved. If a Kutta condition is added, enforcing a zero pressure jump at the trailing edge, the system of matching equations is modified as in François et al. [54] (detailed derivations can be found in Appendix D). The various steps of the modeling procedure, from the geometric definition to the main equations implemented, are summarized in a schematic diagram in Fig. 8.

Before moving on to the mode-matching results in Section 6, the validity of the numerically solved modal basis is assessed in the next section, by comparing its asymptotic behavior to analytical solutions. This gives an understanding of the key elements required for certain comparisons of the mode-matching results.

5. Modal basis asymptotic behavior

5.1. In the limit of small curvature

The numerical solution of the inter-vane channel modal basis ψ and wavenumbers μ from Eq. (34) is first tested in a curved duct without flow (M=0). The frequency is set to kb=12 and the curvature ranges from $b/R_c=0$ to $b/R_c\simeq 0.36$, which corresponds to values of Ψ ranging from 0° to 40° with a solidity of l/b=1.8 for a cascade channel. When the curvature tends to 0, the expected eigenfunctions are cosine functions: $\cos{(q\pi[n+b/2]/b)}$, where q is the mode order. Fig. 9 displays the eigenfunctions ψ_q for q=0

Geometry Extraction of 2D vane profile Vane profile approximation by at a given radius/span mean camber line (modified circle arc) Account for vane stagger and camber, but not thickness Flow $\mathbf{U}(S,n) = U_{0s}(S)\mathbf{e}_s + \epsilon U_{1n}(S,n)\mathbf{e}_n + \mathcal{O}(\epsilon^2)$ Multiple-scale expansion of $D(S, n) = D_0(S) + \mathcal{O}(\epsilon^2)$ the mean flow fields in the inter-vane channels $C(S, n) = C_0(S) + \mathcal{O}(\epsilon^2)$ Account for mean flow deviation and compressibility, but not vane loading or flow angle of attack Acoustic modes Upstream/downstream of the cascade described in Boulev et al. [6] with the addition of a skewed mean flow Linearized Euler equations for an isentropic flow of ideal gas Inter-vane channel modes as in a curved slowly-varying duct from Brambley and Peake [35] Account for inter-vane channel curvature and expansion Mode-matching equations Leading-edge interface: upstream annular modes and staggered inter-vane channel modes Conservation of mass-flow rate and stagnation enthalpy (Dixon and Hall [36]) Trailing-edge interface: inter-vane channel modes, downstream annular modes and a Kutta condition Conservation of Γ_1 at LE Modal truncation of Conservation of Γ_2 at LE I_2 the linear system $\vec{B_q}$ Conservation of Γ_1 at TE 0 to be solved numerically Conservation of Γ_2 at TE 0 Zero pressure jump at TE

Fig. 8. Schematic diagram illustrating the solution method of the present paper.

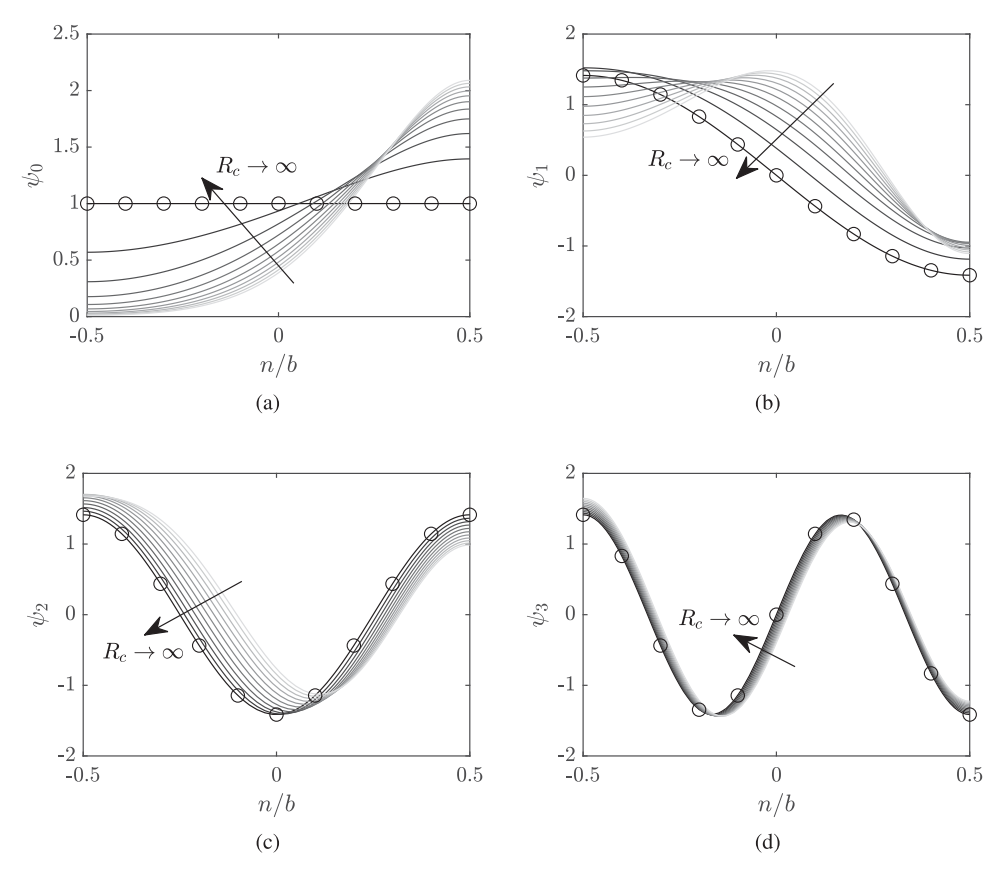


Fig. 9. Eigenfunctions numerically computed for various curvature radii (solid lines) and the analytical cosine function for $b/R_c = 0$ (O). The subfigures (a) to (d) correspond to mode orders q = 0 to 3.

to 3, computed with the collocation algorithm, for the different curvatures in shades of gray. The corresponding cosine functions for $b/R_c = 0$ are added in black circles.

The collocation algorithm is able to recover the analytical solution in the limit of small curvature in all cases. When the curvature increases, the symmetry of the modes with respect to the origin is broken. The nodes (zeros of the eigenfunctions) are pushed toward the upper part of the channel, away from the curvature center. The eigenfunctions also tend to have a larger amplitude at the bottom of the channel, for $q \ge 2$, whereas the amplitude concentrates near the middle for q = 1, and at the top for q = 0. The asymmetry is no longer visible beyond a given mode order, which increases with curvature. Consequently, curvature only affects significantly a finite number of the lower-order modes.

Fig. 10 shows the eigenvalue evolution of the cut-on modes (Fig. 10(a)) and of the first four cut-off modes (Fig. 10(b)). The plots start at a cross mark $(b/R_c = 0)$ and end at a square mark $(b/R_c \simeq 0.36)$. The analytical values for $b/R_c = 0$ are added in black circles, as $\mu_a = \sqrt{k^2 - (q\pi/b)^2}$.

Again, the analytical solution is recovered in the limit $b/R_c \rightarrow 0$, and the effect of curvature decreases rapidly with mode order (only the first 3 modes are significantly affected in this example). The cut-off modes are then naturally less affected by curvature due to their higher order. Furthermore they can be significant only over a reduced channel extent. The concentration of the eigenfunction at the top of the channel observed for the fundamental mode q=0 (Fig. 9(a)) corresponds to what is commonly named a whispering-gallery mode. This is similar to the concentration of high-order azimuthal modes in cylindrical or annular ducts above a specific caustic radius, according to the terminology of Chapman [55]. Fig. 10(a) shows that, unlike the other cut-on modes, the eigenvalue of the fundamental mode increases with curvature. Therefore, its caustic radius is expected to increase with curvature, as shown in Fig. 9(a). Since its eigenvalue also increases in absolute value with frequency and adverse mean flow, the whispering-gallery effect should be stronger in these cases as well, which are presented hereafter.

5.2. In the limit of small mach number

Now the curvature is fixed to $b/R_c=0.36$ and the frequency at kb=12, but the Mach number varies from M=-0.6 to M=0.6 by increments of 0.12. Notice that, due to symmetry in Eq. (34), the eigenfunctions of the left-running modes ψ_q^- for M>0 are the same as the eigenfunctions of the right-running modes ψ_q^+ for M<0. In that regard, only the eigenfunctions ψ_q^+ are presented,

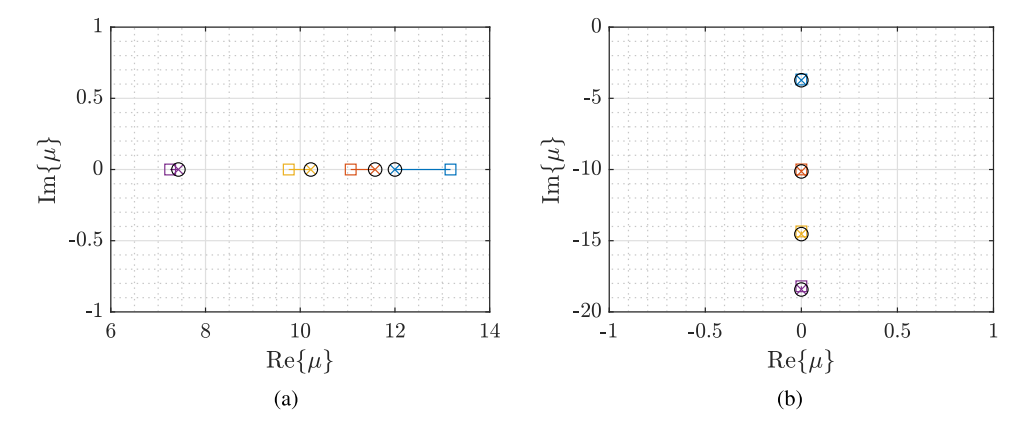


Fig. 10. Eigenvalues of the cut-on modes q = 0 (——), q = 1 (——), q = 2 (——), q = 3 (——) (a), and the first four cut-off modes q = 4 (——), q = 5 (——), q = 6 (——), q = 7 (——) (b) for various curvature values. Cross marks at $b/R_c = 0$ and square marks at $b/R_c \simeq 0.36$, with the analytical solution added for $b/R_c = 0$ (O).

corresponding to downstream-propagating modes when M > 0 and upstream-propagating modes when M < 0, respectively. Fig. 11 depicts the eigenfunctions ψ_q^+ , for q = 0 to 3, computed numerically for the different Mach numbers in shades of gray, where the black solid line corresponds to M = 0. The analytical solution for M = 0, given by the combination of Bessel functions of Eq. (33), is added as black circles.

It appears that the mean flow has a stronger impact on the upstream-propagating modes (M < 0) and, in this case, amplifies the effect of curvature on the mode shapes. On the contrary, the mean flow reduces the effect of curvature on the downstream-propagating modes (M > 0) and its impact vanishes quickly with mode order. It is important to emphasize that this conclusion might be limited to uniform mean flows.

5.3. In the limit of low frequency

To conclude this series of asymptotic comparisons, the limit of the first modes when the frequency tends toward 0 is analyzed, in order to assess the validity of the straight-channel approximation used in Roger et al. [14]. The curvature is set to $b/R_c \simeq 0.36$ and the Mach number to M=0.6 (most critical case). The frequency ranges from $kb\simeq 0$ to kb=12. Fig. 12 displays the eigenfunctions ψ_q , for q=0 to 3, computed with the collocation algorithm (solid lines), for the different frequencies, and the cosine functions for an equivalent straight duct (black circles).

When $kb \to 0$, the first eigenfunction ψ_0 tends to a constant value, similar to the plane-wave mode in a straight duct, because the Laplace equation shares this solution with the Helmholtz equation. However, for all other modes, the limit is not the cosine mode, and the larger the mode order, the larger the difference. Whether or not the approximation by a straight channel of equivalent height expansion is valid then relies on the eigenvalue estimation. Fig. 13 plots the relative difference between μ_0 and its value in an equivalent straight channel: $-k(M \mp 1)/(1 - M^2)$. In this case, the difference is negligible for values of kb of the order of unity. Hence, the straight-channel approximation should be accurate for the fundamental mode as long as the channel length is small compared to the acoustic wavelength. For a longer channel, the cumulative discrepancy of μ_0 integrated along the channel could cause a significant phase difference at the outlet, as was also noticed by Roger and Moreau [17]. That is why neglecting the curvature when computing the channel modal basis [14] can be viewed as a low-frequency approximation. A good rule of thumb for the frequency limit of this approximation is to use the first cut-off frequency of the channels $(kb < \pi)$, keeping in mind that it might break down for lower frequencies if the curvature exceeds those encountered in compressor stages.

6. Comparison of the mode-matching technique with numerical solving

6.1. Methodology

6.1.1. Without flow

The model developed in Section 4 is referred to as Mode Matching for Bifurcated Curved Waveguides (MMBCW) in this study. Test cases are defined in this section to assess its validity against reference numerical simulations. In a first instance, the MMBCW is considered in a medium at rest. The reference results are computed with the commercial software Simcenter 3D Acoustics. This software addresses the two-dimensional Helmholtz problem with a high-order adaptive Finite Element Method (FEM) [56,57]. Only key aspects are mentioned here, details being found in the references. The FEM calculation uses the *a priori* error indicator from Bériot et al. [56] to adjust the order in every element for each frequency. The target error is set to 0.1 percent. Periodic boundary conditions are enforced on the horizontal boundaries, while an active Perfectly Matched Layer (PML) is used to enforce the incoming wave and avoid spurious reflections [58].

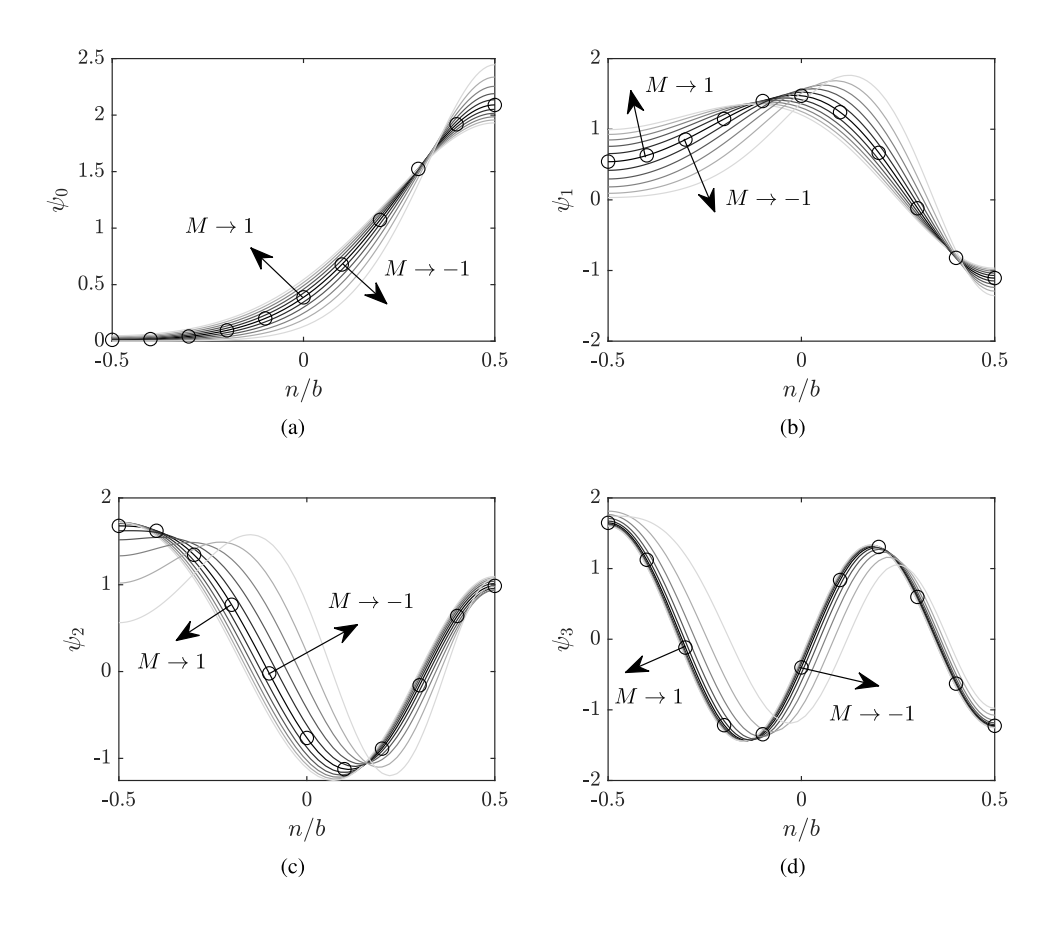


Fig. 11. Eigenfunctions numerically computed for various Mach numbers (solid lines) and the combination of Bessel functions, Eq. (33), for M = 0 (\bigcirc). Positive Mach numbers correspond to downstream-propagating modes, whereas negative Mach numbers correspond to upstream-propagating modes. The subfigures (a) to (d) correspond to mode orders q = 0 to 3.

Table 1 Input parameters of the test case without flow, $D_{ref} = 1.225 \text{ kg/m}^3$ and $C_{ref} = 340 \text{ m/s}$.

V	Ψ (deg)	l/b	b/R_c	$M_{-\infty}$	$D_{-\infty}/D_{\mathrm{ref}}$	$C_{-\infty}/C_{\mathrm{ref}}$
4	30	1.04	0.5	0	1	1

The first test case is focused on the curvature effects and the validity of the slowly-varying potential. For that matter, the same vane geometry is used in the numerical simulations and comparisons are also made with the straight-channel approximation of Ref. [14], called hereafter: Mode Matching for Bifurcated Waveguides (MMBW). The test case is defined as follow. A cascade of four vanes (V=4) is considered at a duct radius of R=38 mm, which gives a vane spacing $b=2\pi R/V\simeq 60$ mm. The camber angle is set at $\Psi=30^\circ$ and the solidity at l/b=1.04. The dimensionless curvature is therefore $b/R_c\simeq 0.5$, which is not small enough to know a priori whether the multiple-scale approximation is appropriate or not. No mean flow is considered (M=0) and the mean density and sound speed are assumed constant and set to D=1.225 kg/m³ and C=340 m/s. Incident acoustic waves of unit amplitude are scattered by the stator vanes. Computations are performed for two couples of frequencies and mode orders: j=1 at kb=2.4289 ($f\simeq 2200$ Hz) and j=5 at kb=12.145 ($f\simeq 11000$ Hz). The mode orders j are chosen so that the propagation angle of the mode is the same in both computations, restricting the analysis to the effect of frequency for a given vane camber. The mesh used in the FEM is displayed in Fig. 14 and the parameters of the test case are gathered into Table 1.

As a second test case, the geometrical approximation of a circle arc used in the MMBCW is evaluated by comparisons with simulations on a realistic cascade. The geometry of the NASA Source Diagnostic Test (SDT) baseline configuration at mid-span is chosen for the numerical simulations [59]. Computations are performed with the MMBCW using two different approximate vane geometries, the so-called: stagger-angle geometry and camber-angle geometry (Fig. 15). The camber-angle geometry has the same camber angle $\Psi = 33.7^{\circ}$ than the SDT, in order to fit the inclination of the vane (and of the equivalent dipoles) at the leading edge. It has therefore a larger stagger angle of 16.8° than the real stagger angle of 11° , and a slightly higher solidity value

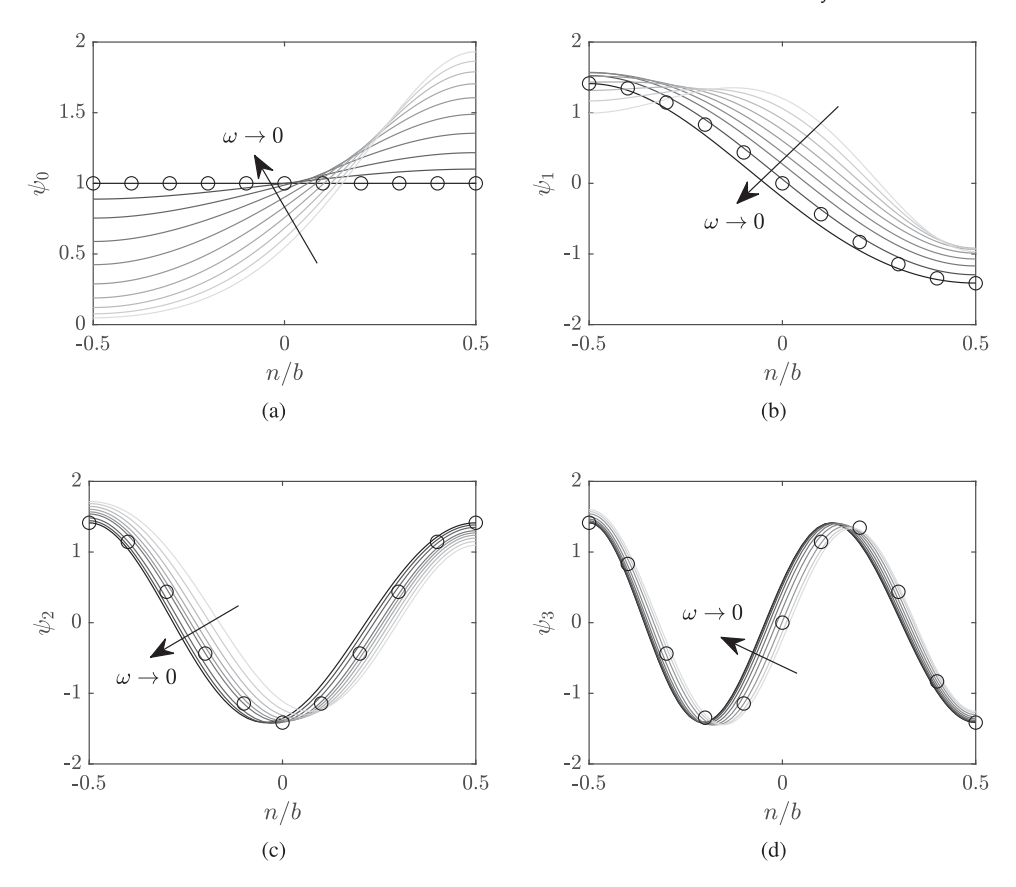


Fig. 12. Eigenfunctions numerically computed for various frequencies (solid lines) and the cosine functions of an equivalent straight duct for $kb \simeq 0$ (O). The subfigures (a) to (d) correspond to mode orders q = 0 to 3.

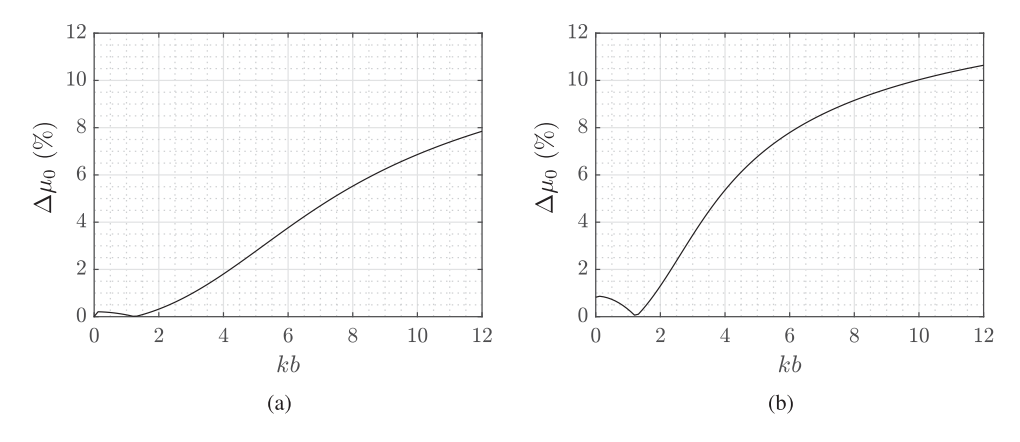


Fig. 13. Relative difference between μ_0 and its value in an equivalent straight channel: $-k(M\mp1)/(1-M^2)$, as a function of frequency: downstream-propagating mode (a); upstream-propagating mode (b).

 $I/b \simeq 1.58$. The stagger-angle model has instead the same stagger angle of 11°, but a substantially lower camber angle ($\Psi = 22^{\circ}$). The dimensionless curvatures are equal to 0.37 and 0.25, respectively. The parameters of the different configurations are reminded in Table 2. Computations are performed for two incident acoustic waves: mode order j = 6 at $kb \simeq 2.75$ (f = 5726 Hz) and mode order j = -18 at $kb \simeq 5.50$ (f = 11452 Hz). The numerical simulations for this test case are also performed with the commercial software Simcenter 3D Acoustics. The mesh used in the FEM is displayed in Fig. 16 with the PML highlighted in blue. The mesh is refined in the region of the blades to guarantee an accurate representation of the geometry in the numerical model.

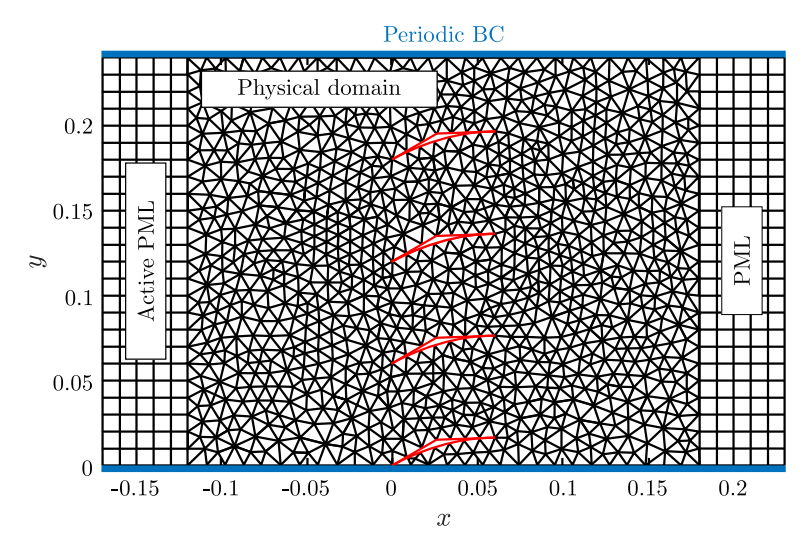


Fig. 14. Explanatory scheme of the numerical setup displaying the geometry, the mesh and how boundary conditions are defined.

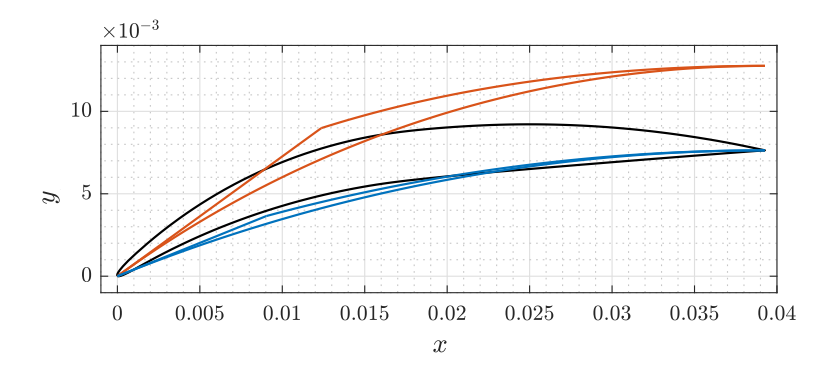


Fig. 15. SDT baseline geometry (——) used in the FEM compared to the approximate vane geometries used in the MMBCW: stagger-angle geometry (——) and camber-angle geometry (——).

Table 2 Input parameters of the realistic test case without flow, $D_{ref} = 1.225 \text{ kg/m}^3$ and $C_{ref} = 340 \text{ m/s}$.

	V	Ψ (deg)	Ψ_s (deg)	l/b	b/R_c	$M_{-\infty}$	$D_{-\infty}/D_{\mathrm{ref}}$	$C_{-\infty}/C_{\mathrm{ref}}$
SDT	54	33.7	11.0	1.54	-	0	1	1
Stagger	54	22.0	11.0	1.54	0.25	0	1	1
Camber	54	33.7	16.8	1.58	0.37	0	1	1

For each configuration, qualitative and quantitative comparisons between FEM and mode-matching results in terms of real values of the fluctuating pressure are presented. Reflected and transmitted acoustic powers are also computed from both numerical and analytical results in order to (i) ensure that the power balance is correctly predicted and (ii) attest the accuracy of the model by checking the energy conservation between the incident power and the sum of the reflected and transmitted powers.

6.1.2. With flow

The validity of the predicted overall mean-flow evolution through the cascade is first assessed without acoustic perturbation. As a reminder, the flow is assumed to be uniform in each cross-section of the channel, and to vary slowly along the channel centerline due to cross-section variations. The inviscid mean flow computed with TURBO [60], presented by Envia for the 4th NASA CAA workshop, category 3, problem 2 [47], is used as a reference result. The test-case parameters are those of the SDT baseline

¹ The same mean flow description is used in both MMBW and MMBCW since the effects of curvature on the mean flow are neglected.

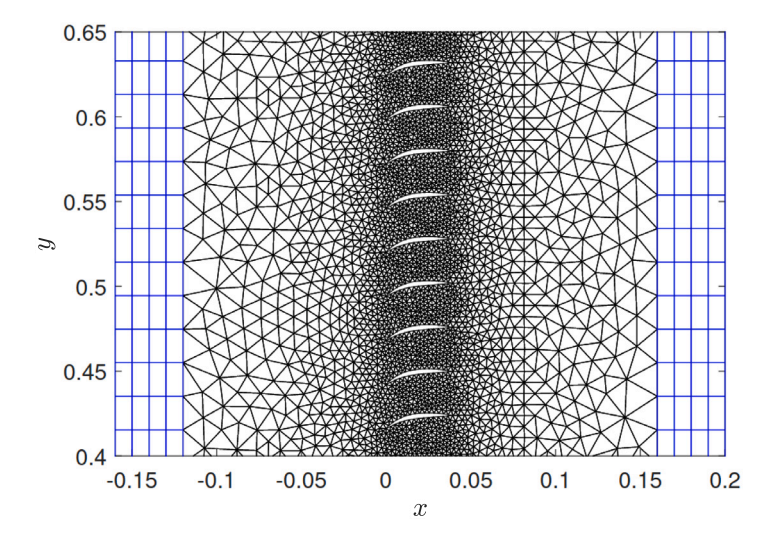


Fig. 16. FEM mesh of the SDT test case without flow.

Table 3 Input parameters of the mean-flow test case, $D_{ref} = 1.225 \text{ kg/m}^3$ and $C_{ref} = 340 \text{ m/s}$.

				10			101		
	V	Ψ (deg)	Ψ_s (deg)	1/b	b/R_c	$M_{-\infty}$	$D_{-\infty}/D_{\mathrm{ref}}$	$C_{-\infty}/C_{\mathrm{ref}}$	Flow angle (deg)
SDT	54	33.7	11.0	1.54	-	0.44958	0.90567	0.98038	36.0
Geom	54	33.7	16.8	1.58	0.37	0.44958	0.90567	0.98038	33.7
Flow	54	36.0	18.0	1.59	0.39	0.44958	0.90567	0.98038	36.0

Table 4 Input parameters of the realistic test case with flow, $P_{ref} = 101325$ Pa.

	V	Ψ (deg)	Ψ_s (deg)	l/b	b/R_c	$M_{-\infty}$	$P_{-\infty}/P_{\mathrm{ref}}$
SDT	54	33.7	11.0	1.54	-	0.4	0.714285
MMBCW	54	33.7	16.8	1.58	0.37	0.4	0.714285

configuration at mid-span and are detailed in Table 3 with the label "SDT". Since the geometry is approximated in the mode-matching model, two configurations are tested in order to define guidelines for tuning the parameters: the so-called geometrical configuration (Geom) and the flow configuration (Flow). The former is identical to the "camber" geometry of the previous test case, whereas the latter ensures the same incident flow angle as in the numerical simulation. Both configurations are also detailed in Table 3.

In the end, the results of acoustic scattering obtained with the MMBCW are compared with those from Hixon [18] to assess the performance of the model in presence of a mean flow. Hixon's results were computed with the NASA Broadband Aeroacoustic Stator Simulation (BASS) code. The BASS code solves the two-dimensional nonlinear Euler equations in the time domain using an explicit fourth-order time marching scheme combined with high-order spatial differencing schemes. The unsteady pressure field is then recovered by subtracting the averaged flow from the instantaneous flow, since the disturbance is so small that the solution is essentially linear in this case. The mean flow has zero incidence angle in Hixon's simulations [18], thus the choice of the camber angle in the MMBCW is straightforward. The parameters for this test case are collected in Table 4. Computations are performed at a fixed frequency kb = 2.75 (f = 5726 Hz), for two mode orders: j = 6 and j = -12. Note that, due to some uncertainties on the simulation parameters and the lack of extracted pressure profiles in Ref. [18], these comparisons are only qualitative.

6.2. Results

6.2.1. Curvature effects

The instantaneous pressure maps computed with the FEM and MMBCW on the academic test case, for j = 1 at kb = 2.4289, are presented in Fig. 17. The locations of the extracted pressure profiles are indicated with dashed black lines and the profiles are plotted in Fig. 18, with the addition of the results obtained with the MMBW.

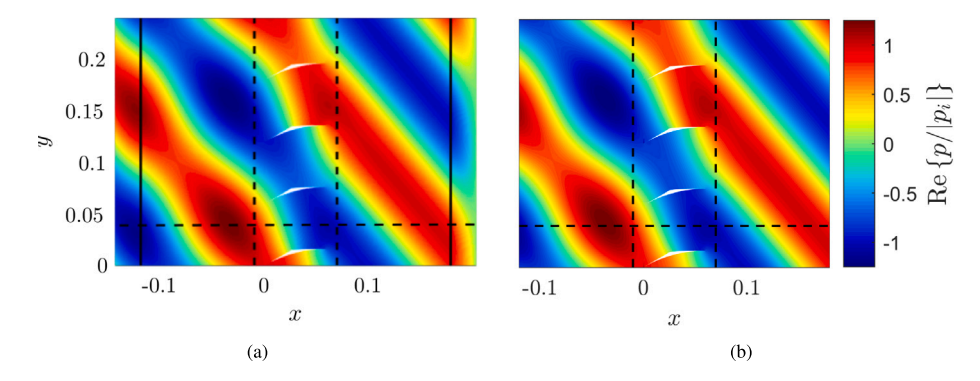


Fig. 17. Instantaneous pressure maps normalized by the incident pressure at origin $|p_i|(x = 0, y = 0)$, computed with FEM (a) and MMBCW (b) for j = 1 at kb = 2.4289. Dashed black lines are the locations for quantitative comparisons and solid black lines in (a) show the limits of PML. (For interpretation of the references to color in this figure legend, the reader is referred to the web version of this article.)

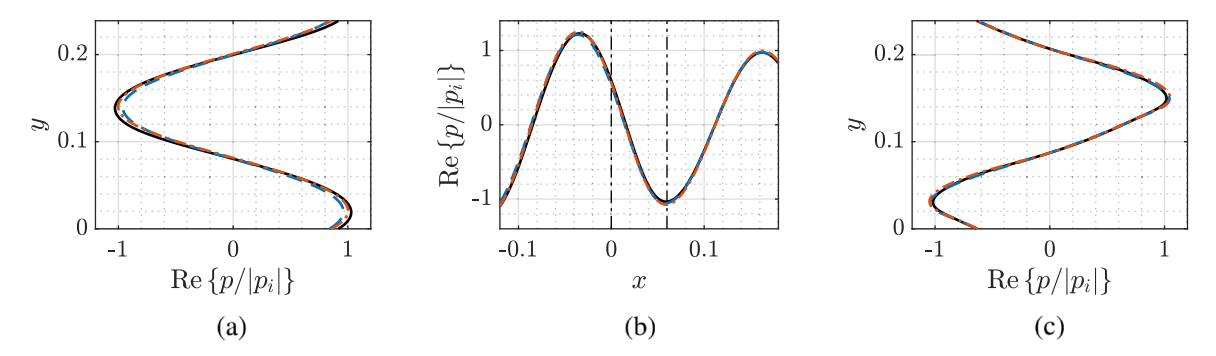


Fig. 18. Instantaneous pressure profiles computed with FEM (\longrightarrow), MMBW (--) and MMBCW (--) for j=1 at kb=2.4289, extracted at x=-0.01 m (a), y=0.04 m (b) and x=0.07 m (c) from Fig. 17. The vertical dash-dotted lines in (b) represent the LE and TE interfaces.

Table 5 Comparison of the reflected \mathcal{P}_r and transmitted \mathcal{P}_t powers, relative to the incident power \mathcal{P}_i , and of the relative conservation error $E = 1 - (\mathcal{P}_t - \mathcal{P}_r)/\mathcal{P}_i$ for j = 1 at kb = 2.4289.

	P_r (%)	P_{t} (%)	E (%)
FEM	5.270	94.62	0.1100
MMBW	4.926	95.06	0.0140
MMBCW	5.200	96.32	-1.520

The MMBCW is in good agreement compared to the FEM results, with a slightly better estimation of the reflected field amplitude compared to the MMBW, in view of Fig. 18(a). The frequency of the test being below the first channel cut-off frequency, the straight-channel approximation is relevant here (see Section 5.3). In other words, this confirms that curvature effects on sound propagation are negligible at low frequency, at least below the first channel cut-off frequency ($kb < \pi$).

The radiated acoustic powers are also computed for the MMBCW and compared to those of the MMBW and FEM in Table 5. This confirms that the reflected power is slightly better estimated with the MMBCW, but also indicates that the MMBCW is less accurate than the MMBW in terms of power balance in this case. The MMBCW results are not significantly improved by increasing the number of modes in the modal truncation. This suggests that some lack of accuracy can be attributed at low frequency either to the numerical computation of the channel modes or to the physical assumptions made in the MMBCW.

When increasing the frequency to kb = 12.145 and changing the incident mode order to j = 5, the MMBCW is still able to recover the pressure pattern of the FEM (Fig. 19).

The pressure profiles extracted upstream, downstream and through the vane cascade are presented in Fig. 20 for the FEM, MMBW and MMBCW. Again, the MMBCW results agree well with the FEM results, whereas the MMBW cannot accurately predict the scattered field downstream of the cascade. The origin of the difference is in the propagation inside the inter-vane channels, as shown by the discrepancies in the MMBW starting at about two thirds of the channel length (Fig. 20(b)). Though there are still some discrepancies in amplitude with the MMBCW, the phase is well predicted downstream (Fig. 20(c)), which suggests that the modal distribution should also be. The balance of acoustic power now reaches the validity target 1% (Table 6). The MMBCW is also able to correctly recover the reflected power that is totally missing in the MMBW.

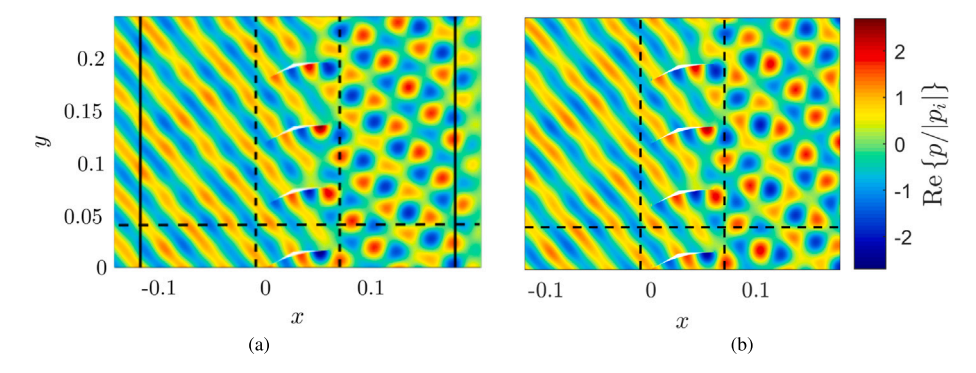


Fig. 19. Instantaneous pressure maps normalized by the incident pressure at origin $|p_i|(x=0,y=0)$, computed with FEM (a) and MMBCW (b) for j=5 at kb=12.145. Dashed black lines are the locations for quantitative comparisons and solid black lines in (a) show the limits of PML. (For interpretation of the references to color in this figure legend, the reader is referred to the web version of this article.)

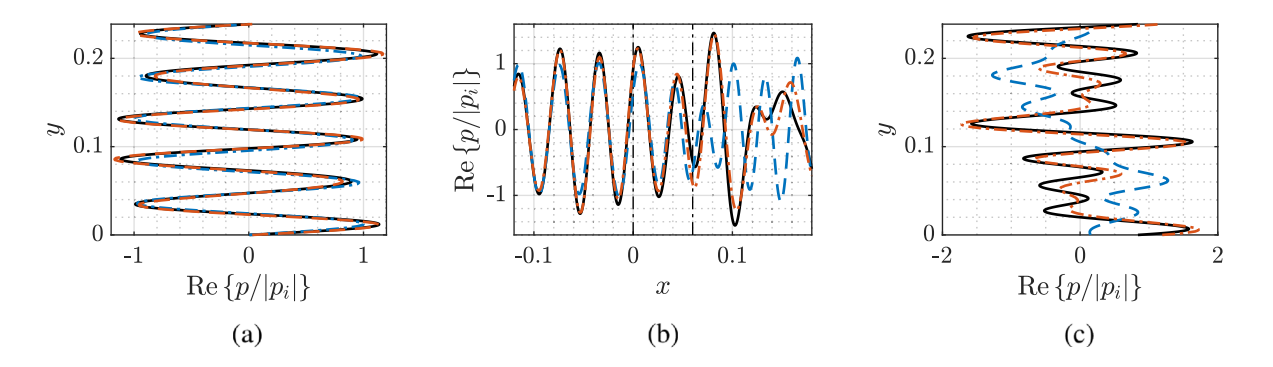


Fig. 20. Instantaneous pressure profiles computed with FEM (\longrightarrow), MMBW (--) and MMBCW (--) for j=5 at kb=12.145, extracted at x=-0.01 m (a), y=0.04 m (b) and x=0.07 m (c) from Fig. 19. The vertical dash-dotted lines in (b) represent the LE and TE interfaces.

Table 6 Comparison of the reflected \mathcal{P}_r and transmitted \mathcal{P}_t powers, relative to the incident power \mathcal{P}_i , and of the relative conservation error $E = 1 - (\mathcal{P}_t - \mathcal{P}_r)/\mathcal{P}_i$ for j = 5 at kb = 12.145.

	\mathcal{P}_r (%)	\mathcal{P}_{t} (%)	E (%)
FEM	3.950	96.05	< 0.01
MMBW	0.301	99.70	-0.001
MMBCW	2.560	96.61	0.830

These results of the academic test case without flow demonstrate the validity of the developed mode-matching model and the relative importance of the curvature effects on sound propagation. They also show that the slowly-varying duct approach is well suited. This new model shows promising capabilities at the cost of a reasonably higher computation time than with the MMBW, say a couple of seconds on a personal laptop.

6.2.2. Geometrical approximation effects

In the previous analysis, numerical simulations were performed using the same geometry as in the mode-matching model. Here, the geometrical approximations in the model are tested on the SDT test case defined in Table 2, again without mean flow. Fig. 21 shows the instantaneous pressure fields obtained at kb = 2.75, with the incident mode order j = 6, for the FEM on the SDT geometry and the MMBCW on the approximate geometries, using the same camber angle or the same stagger angle. The extracted pressure profiles are then presented in Fig. 22.

The scattered sound field is well reproduced by the modified circle arc geometry used in the mode-matching procedure in this case, using either the stagger-angle or the camber-angle geometry. Yet, the approximate vane geometry with the real camber angle gives a slightly better amplitude inside the inter-vane channels and upstream of the vanes, compared to the geometry using the real stagger angle. Since the camber-angle geometry is more representative of the real geometry at the leading edge, the reflected field is expected to be more accurate. However, downstream of the cascade, using either geometry makes no difference at this frequency.

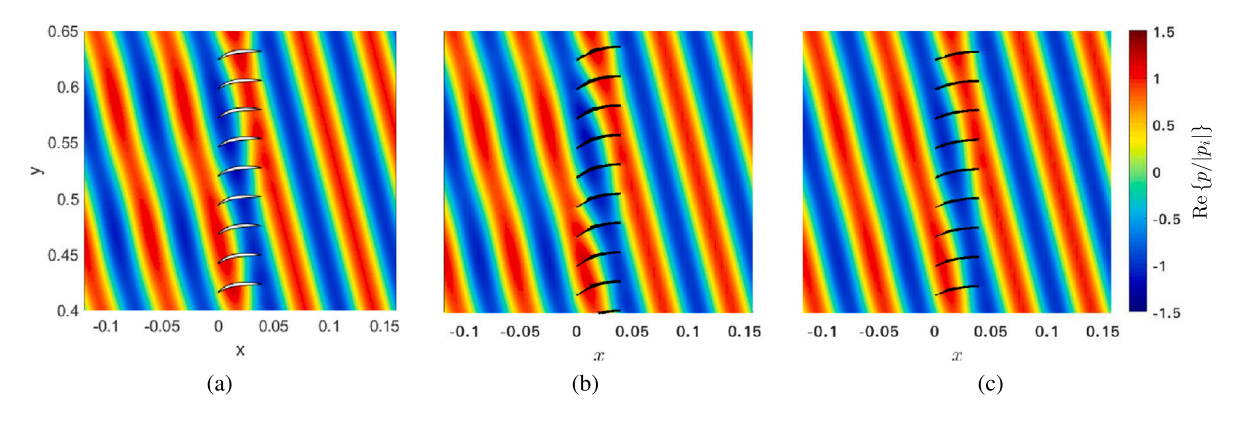


Fig. 21. Instantaneous pressure maps normalized by incident pressure at origin $|p_j|(x=0, y=0)$, computed with FEM (a), MMBCW/Camber (b) and MMBCW/Stagger (c) for j=6 and kb=2.75. (For interpretation of the references to color in this figure legend, the reader is referred to the web version of this article.)

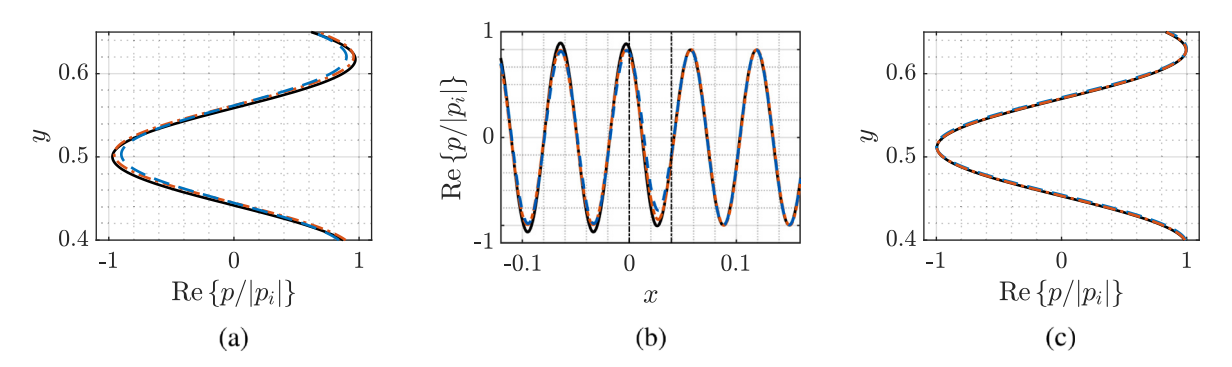


Fig. 22. Instantaneous pressure profiles computed with FEM (——), MMBCW/Stagger (——) and MMBCW/Camber (——) for j = 6 at kb = 2.75, extracted at x = -0.04 m (a), y = 0.013 m (b) and x = 0.08 m (c) from Fig. 21. The vertical dash-dotted lines in (b) represent the LE and TE interfaces.

Table 7 Comparison of the reflected \mathcal{P}_r and transmitted \mathcal{P}_t powers, relative to the incident power \mathcal{P}_i , and of the relative conservation error $E = 1 - (\mathcal{P}_t - \mathcal{P}_r)/\mathcal{P}_i$ for j = 6 at kb = 2.75.

	\mathcal{P}_r (%)	\mathcal{P}_{t} (%)	E (%)
FEM	0.951	99.06	-0.011
MMBCW/Stagger	0.190	99.67	0.140
MMBCW/Camber	1.080	99.37	-0.450

These observations are confirmed by Table 7, which shows the reflected and transmitted acoustic powers, as well as the conservation error, for the FEM and both approximate geometries. It also highlights that the difference between the approximate geometries lies mainly in the reflected field, and that the MMBCW can achieve good accuracy in a realistic test case.

Figs. 23 and 24 display the results for twice the frequency (kb = 5.5), and with an incident mode order j = -18.

Discrepancies between the analytical and numerical solutions are more significant at this frequency. This is expected since high frequency waves are more sensitive to small details of the vane geometry. Nevertheless, the predicted pressure field from the MMBCW is still in good agreement with the FEM result. The camber-angle geometry gives better results, especially upstream of the vanes where the stagger-angle geometry seems to miss a cut-on reflected mode. Fig. 24(a) shows that the stagger-angle geometry predicts a sinuous pattern in the reflected field, thus dominated by a single mode, whereas the camber-angle geometry correctly reproduces the disturbed sine wave, representative of a stronger reflection. Table 8 confirms this result, indicating a reflected power two times stronger with the camber-angle geometry, which is closer to the FEM result.

Up to the frequency kb = 5.5, the modified circle arc geometry used in the model is able to generate a pressure field in fairly good agreement with the FEM results on a realistic geometry. This is encouraging for reliable and fast sound predictions in an industrial context, typically if repeated calculations are required, to predict broadband noise within the scope of a statistical approach or to run an optimization algorithm. The geometry mimicking the same camber angle should be preferred, as it reproduces more precisely the reflected scattered waves, as well as both reflected and transmitted powers.

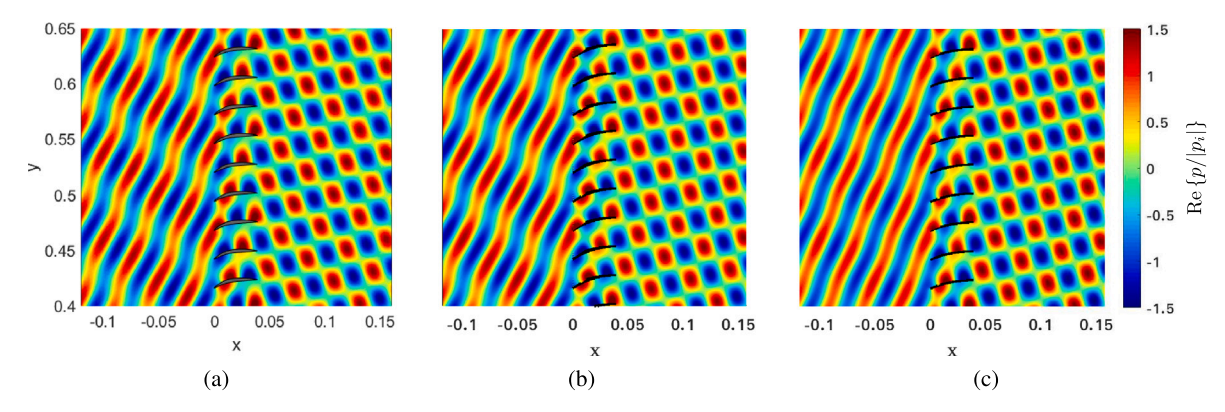


Fig. 23. Instantaneous pressure maps normalized by incident pressure at origin $|p_i|(x=0,y=0)$, computed with FEM (a), MMBCW/Camber (b) and MMBCW/Stagger (c) for j=-18 and kb=5.5. (For interpretation of the references to color in this figure legend, the reader is referred to the web version of this article.)

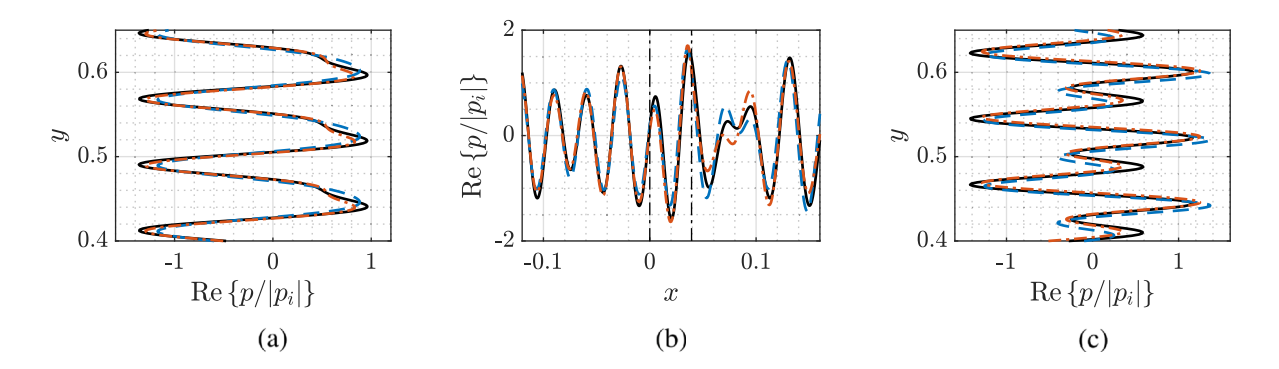


Fig. 24. Instantaneous pressure profiles computed with FEM (——), MMBCW/Stagger (——) and MMBCW/Camber (——) for j = -18 and kb = 5.5, extracted at x = -0.04 m (a), y = 0.013 m (b) and x = 0.08 m (c) from Fig. 23. The vertical dash-dotted lines in (b) represent the LE and TE interfaces.

Table 8 Comparison of the reflected \mathcal{P}_r and transmitted \mathcal{P}_t powers, relative to the incident power \mathcal{P}_t , and of the relative conservation error $E = 1 - (\mathcal{P}_t - \mathcal{P}_r)/\mathcal{P}_t$ for j = -18 at kb = 5.50.

	P_r (%)	\mathcal{P}_{t} (%)	E (%)
FEM	10.57	89.43	< 0.01
MMBCW/Stagger	4.420	95.37	0.210
MMBCW/Camber	9.620	90.58	-0.200

6.2.3. Mean flow approximation effects

The inviscid mean flow description used in the mode-matching model is compared to the inviscid mean flow computed with TURBO [60], from the 4th NASA CAA workshop, category 3, problem 2 [47]. Fig. 25 shows the qualitative numerical and analytical mean flow evolution through the cascade (using the "Flow" configuration). Table 9 presents the quantitative results downstream of the cascade, as well as the difference between the analytical and numerical results indicated by the Δ symbol (in percentage of the numerical value).

The mean flow quantities downstream of the cascade are well recovered by the analytical model using the geometry optimized for the flow description (Flow), whereas the true vane geometry (Geom) suffers from a relative error of more than 3% on the Mach number. Both geometries give accurate changes of mean density and sound speed. These results demonstrate that the overall change in the inviscid mean flow through a realistic cascade of vanes is mainly due to the cross-section variations of the inter-vane channels, and is well recovered by a nearly uniform mean-flow description neglecting curvature and mean loading effects. However, when looking at local variations of the mean flow in the vicinity of the vanes, the nearly uniform mean-flow description is clearly inadequate.

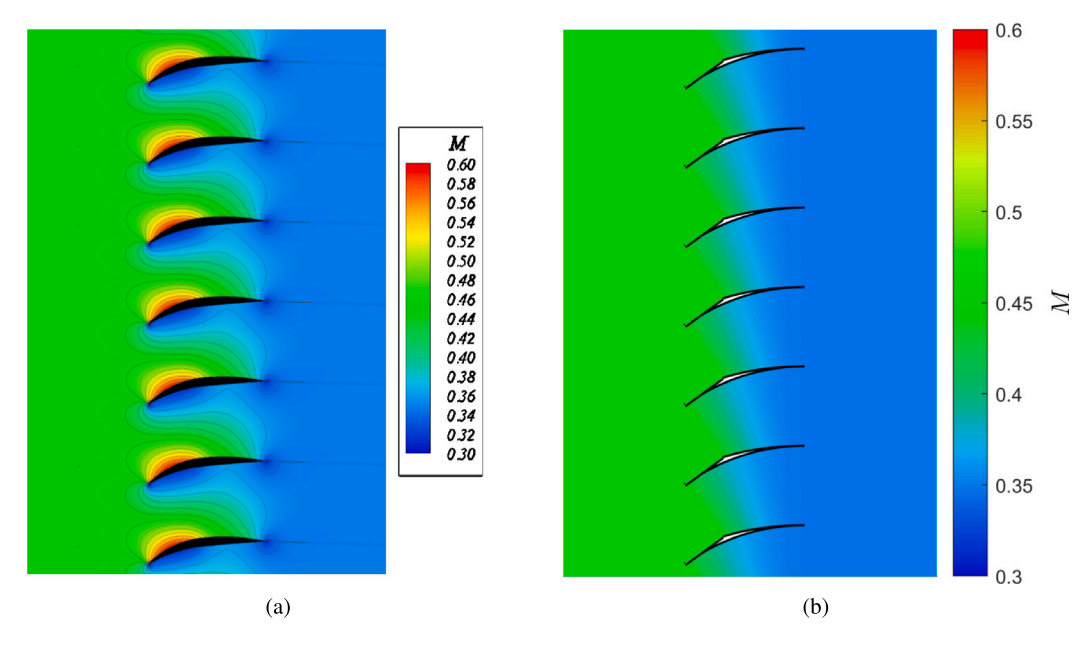


Fig. 25. Qualitative comparison of the total Mach number from Ref. [60] (a) and the analytical description used in the mode-matching models (b) for input parameters defined in Table 3. Color scales are not equal. (For interpretation of the references to color in this figure legend, the reader is referred to the web version of this article.)

Table 9Mean flow quantities downstream of the cascade computed with TURBO on the SDT geometry, and analytical mean flow quantities predicted with a uniform flow using the geometrical and flow configurations. Input parameters defined in Table 3.

	$M_{+\infty}$	$D_{+\infty}/D_{\mathrm{ref}}$	$C_{+\infty}/C_{\mathrm{ref}}$	ΔM (%)	$\Delta \left(D/D_{\mathrm{ref}}\right)$ (%)	$\Delta \left(C/C_{\mathrm{ref}} \right)$ (%)
SDT	0.34704	0.94216	0.98817	0.0000	0.0000	0.0000
Geom	0.35836	0.93856	0.98740	3.2619	0.3821	0.0779
Flow	0.34682	0.94229	0.98818	0.0634	0.0138	0.0010

6.2.4. Comparisons of acoustic scattering with flow

Finally, Figs. 26 and 27 display the pressure fields computed with BASS [18] and with the MMBCW (imposing a Kutta condition as defined in Ref. [54], and detailed in Appendix D) at kb = 2.75 and with $M_{-\infty} = 0.4$, for the incident mode orders j = 6 and j = -12. The parameters are detailed in Table 4. TURBO solves the steady part of the same nonlinear Euler equations as BASS, except that TURBO is a 3-D solver, whereas BASS is 2-D. Although the mean flow description computed with BASS is not provided in Ref. [18], it should be fairly the same as in Fig. 25(a).

In both cases, the pressure field from the MMBCW is in a good qualitative agreement with the numerical simulations. The inclination and relative phase of the scattered waves are well reproduced upstream and downstream of the cascade. The amplitude of the reflections also seems correctly predicted when looking at the wiggly interference pattern of the pressure field, but might still be slightly underestimated in Fig. 26(b). In Fig. 27(a), downstream of the cascade, the pressure field is polluted by spurious numerical reflections at the exit boundary as explained by Hixon [18]; this result was presented as an example of such an issue with Giles 'nonreflecting' boundary conditions. Only a single cut-on mode should propagate, as predicted by the mode-matching model in Fig. 27(b).

Although only qualitative, these results are highly satisfactory and encouraging. They show that the model of sound reflection and transmission performs well, even in the presence of a mean flow, and that the assumption of nearly-uniform mean flow can give relevant acoustic results in this case.

6.3. Discussion

The results support the statement that the model based on equivalent straight channels performs well at low frequency, as was pointed out by different authors [17,26]. However, at higher frequencies, the curvature effects are no longer negligible and the straight-channel approximation induces an artificial deviation of the wavefronts through the cascade, possibly ending up to a shifted dominant mode order downstream of the cascade.

These results also demonstrate the validity of the slowly-varying duct approach, and of the channel modal basis approximation in the triangle ABC. Furthermore, the geometrical approximation of the vane profile (circle arc with artificial thickness) is shown

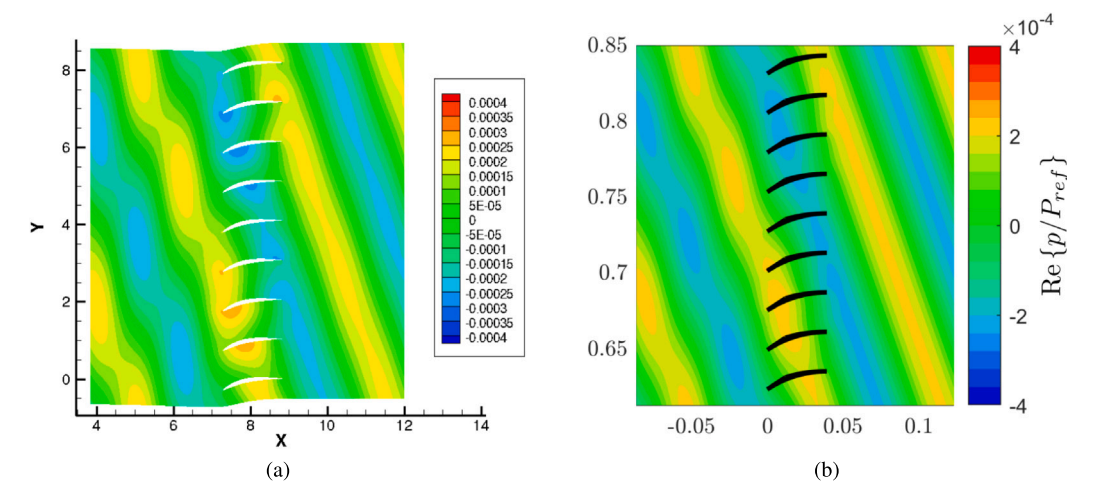


Fig. 26. Instantaneous pressure maps normalized by $P_{\text{ref}} = 101325$ Pa, from Ref. [18] (a) and MMBCW with a Kutta condition (b) for j = 6 at kb = 2.75, $M_{-\infty} = 0.4$. Color scales are not equal. (For interpretation of the references to color in this figure legend, the reader is referred to the web version of this article.)

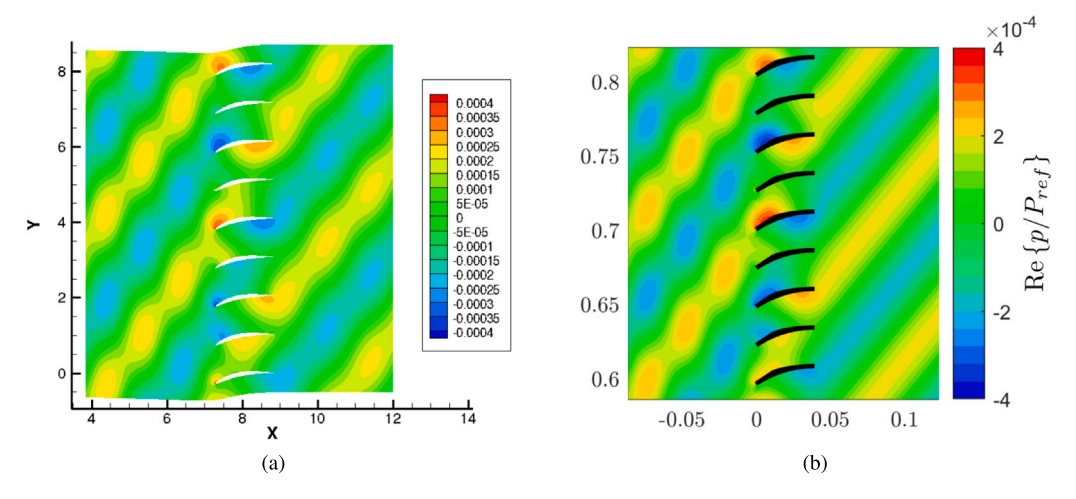


Fig. 27. Instantaneous pressure maps normalized by $P_{\rm ref} = 101325$ Pa, from Ref. [18] (a) and MMBCW with a Kutta condition (b) for j = -12 at kb = 2.75, $M_{-\infty} = 0.4$. Color scales are not equal. (For interpretation of the references to color in this figure legend, the reader is referred to the web version of this article.)

to give reasonable results when used on the SDT test case at mid-span. Nonetheless, comparisons have been performed at relatively low and moderate frequencies only (kb = 2.75 and kb = 5.5), which would barely cover the first four harmonics of the blade passing frequency in the SDT baseline configuration (7808 RPM). Geometrical discrepancies between the model and the real vane profile will have more and more impact as the frequency increases. Further investigations are needed to assess the sensitivity of the two-parts circle arc model at higher frequencies.

Regarding the acoustic field in the presence of a mean flow, the analytical predictions are in good qualitative agreement with numerical results. Yet, no quantitative comparisons were made and the numerical results are available at low frequency only (kb = 2.75). Further investigations are also needed to release this limitation.

7. Conclusion

A two-dimensional model of acoustic scattering by a cascade of cambered vanes was developed, based on the mode-matching technique for periodic bifurcated waveguides. Comparisons with high-fidelity numerical simulations were performed to assess the validity of the assumptions made on the geometry and on the flow. It was also proved to be necessary to account for curvature above the first channel cut-off frequency, as a condition for relevant predictions of the acoustic field downstream of the cascade, as well as of the radiated acoustic powers upstream and downstream.

Compared to the previous implementation of mode-matching for bifurcated waveguides [14], the computation time is still affordable for parametric studies and/or uses in optimization loops in an industrial context: a few seconds on a personal laptop for a given incident mode at a specific frequency.

The mean-flow approximation has shown to accurately reproduce the overall change in the mean-flow quantities from upstream to downstream. However, the local description in the inter-vane channels and near the stator vanes cannot reproduce the details of numerical inviscid computations. This local difference is mainly due to the mean loading of the vanes, which generates a non-uniform mean flow. It would be interesting to compare the results of acoustic scattering with a uniform mean flow and a rotational-free sheared mean flow inside the inter-vane channels, as a non-uniform mean flow is expected to have a significant influence at high frequencies, according to Peake and Kerschen [33,34]. Improvements could be made following Rienstra's work [44] for the velocity potential in the inter-vane channels. Additional numerical results would also be useful for quantitative comparisons in presence of a mean flow.

Another path for improvements is the extension to three dimensions with staggered vanes, and then with cambered vanes. How to cope with the inter-vane geometry definition is still to be dealt with, as well as deciding whether or not such an approach is more relevant than the use of radial strips. The computation time of the Chebyshev collocation method might also become prohibitive for optimization strategies or for use in broadband-noise prediction schemes.

Currently undergoing works, based on the present MMBCW model, are investigating the effects of vane camber on acoustic resonances. They also address the cut-on/cut-off mode transitions, as a consequence of the variation in inter-vane channel cross-section. These topics were discarded from the present analysis, focused on fundamental aspects, for the sake of brevity.

CRediT authorship contribution statement

Léo Girier: Writing – review & editing, Writing – original draft, Visualization, Validation, Software, Resources, Methodology, Investigation, Formal analysis, Data curation, Conceptualization. **Michel Roger:** Writing – review & editing, Validation, Supervision, Resources, Project administration, Funding acquisition, Conceptualization. **Hadrien Bériot:** Writing – review & editing, Software, Resources.

Declaration of competing interest

The authors declare that they have no known competing financial interests or personal relationships that could have appeared to influence the work reported in this paper.

Acknowledgments

This work was performed within the framework of the industrial chair ARENA (ANR-18-CHIN-0004-01) co-financed by Safran Aircraft Engines and the French National Research Agency (ANR), with the help of the French governmental plan "France Relance", and is also supported by the Labex CeLyA of the Université de Lyon, operated by the ANR (ANR-10-LABX-0060/ANR-16-IDEX-0005).

Appendix A. Conservation laws with an oblique mean flow

The mass conservation at an interface between a sub-domain 1 and a sub-domain 2 translates to mass-flow conservation through the interface as

$$\left[\rho^* \mathbf{u}^*\right]_1^2 \cdot \mathbf{n} = 0,\tag{A.1}$$

where $[\bullet]_1^2$ represents the difference between values of the quantity in domains 2 and 1, and n is the normal unit vector to the interface. Linearization yields

$$\left[\rho U_{x} + Du_{x}\right]_{1}^{2} = 0. \tag{A.2}$$

Because the mean velocity is equal on both sides of the interface, the mean density is also constant. This allows the use of the isentropic relation: $p = \rho C^2$. Multiplying Eq. (A.2) by the Mach number $M_x = U_x/C$, and dividing by the mean density D finally gives

$$\left[\frac{p}{Z}M_x^2 + M_x u_x\right]_1^2 = 0,\tag{A.3}$$

where Z = DC

Across the stator, no external work acts on the fluid. Since the flow is assumed inviscid and adiabatic, hence isentropic, the combined conservation of momentum and energy is equivalent to the conservation of total (or stagnation) enthalpy [36]:

$$\left[H^* + \frac{1}{2}|\mathbf{u}^*|^2\right]_1^2 = 0,\tag{A.4}$$

where

$$|\mathbf{u}^*|^2 = (U_v + u_v)^2 + (U_v + u_v)^2.$$
 (A.5)

For an ideal gas, the enthalpy can be written as

$$H^* = C_p T + \frac{p}{D},\tag{A.6}$$

where C_p is the heat capacity at constant pressure. Linearization of Eq. (A.4) yields

$$\left[\frac{p}{D} + U_x u_x + U_y u_y\right]_1^2 = 0.$$

Finally, dividing the above equation by the mean sound speed C, identical on both sides of the interface, gives

$$\left[\frac{p}{Z} + M_x u_x + M_y u_y\right]_1^2 = 0. \tag{A.7}$$

Denoting by U the norm of the mean velocity and by Ψ the angle with the direction perpendicular to the interface, the x-axis in Fig. 1, allows one to express the mean velocity components as $U_x = U \cos \Psi$ and $U_y = U \sin \Psi$. The conservation of total enthalpy (A.7) is then recast as

$$\left[\frac{p}{Z} + M_x \left(u_x + u_y \tan \Psi\right)\right]_1^2 = 0. \tag{A.8}$$

Combining Eqs. (A.3) and (A.8) yields the conservation of the fluctuating pressure p and fluctuating axial velocity u_x , commonly used in mode-matching procedures, but only for the particular case where the mean flow is perfectly perpendicular to the interface, i.e. when $\Psi = 0$. In general, when $\Psi \neq 0$ and $M \neq 0$, new variables need to be introduced to ensure the conservation of mass-flow and total enthalpy through the interface.

Due to camber, the leading-edge interface is staggered in the vanes reference frame. The pressure p and fluctuating axial velocity u_x cannot be used as conservative variables. Expanding the linearized conservation of total enthalpy (A.7) leads to

$$\left[ik\phi - M_x u_x - M_v u_v + M_x u_x + M_v u_v\right]_1^2 = \left[ik\phi\right]_1^2 = 0,$$
(A.9)

which simply reduces to the conservation of ϕ . The variable Γ_1 is

$$\Gamma_1 = \phi$$
. (A.10)

The linearized conservation of mass-flow rate (A.3) reads

$$\left[ikM_{x}^{2}\phi + \beta_{x}^{2}M_{x}u_{x} - M_{x}^{2}M_{y}u_{y}\right]_{1}^{2} = 0,$$
(A.11)

where $\beta_x^2 = 1 - M_x^2$. Since the potential continuity is already enforced, this equation reduces to the conservation of the following quantity:

$$\Gamma_2 = \beta_x^2 u_x - M_x M_y u_y, \tag{A.12}$$

composed of the fluctuations of axial and tangential velocities. This variable can also be rewritten as

$$\Gamma_2 = \beta^2 u_v - M^2 u_v \tan \Psi. \tag{A.13}$$

That demonstrates the equivalence of the conservation of Γ_2 and u_x when $\Psi \to 0$ and/or $M \to 0$. In these particular cases, the set of variables (Γ_1, Γ_2) is equivalent to (ϕ, u_x) or (p, u_x) as used for unstaggered flat vanes.

Appendix B. Chebyshev collocation method

In order to formulate a linear eigenvalue problem (according to μ) from Eq. (26), an intermediate variable is introduced as $\psi^* = \mu \psi$. This results in the generalized eigenvalue problem

$$\begin{bmatrix} \mathcal{L} & 0 \\ 0 & 1 \end{bmatrix} \begin{bmatrix} \psi \\ \psi^* \end{bmatrix} = \mu \begin{bmatrix} 2kM/h_s & \beta^2/h_s^2 \\ 1 & 0 \end{bmatrix} \begin{bmatrix} \psi \\ \psi^* \end{bmatrix}, \tag{B.1}$$

where

$$\mathcal{L} := \frac{\partial^2}{\partial n^2} + \frac{1}{h \cdot R} \cdot \frac{\partial}{\partial n} + k^2. \tag{B.2}$$

The first line corresponds to the mode shape Eq. (26), whereas the second line gives the relation between ψ and ψ^* . Chebyshev polynomials are widely used to solve non-periodic partial differential equations due to their mathematical properties and exponential convergence (see for example Ref [61]. Chapter 2.4 for details). For $-1 \le x \le 1$, the Chebyshev polynomials of the first kind are defined by

$$T_m(x) = \cos(m\bar{x}), \quad \bar{x} = \arccos(x), \quad 0 \le m < \infty.$$

The Chebyshev expansion of a function f, defined on the interval [-1, 1], is

$$f(x) = \sum_{m=0}^{\infty} \hat{f}_m T_m(x), \quad \hat{f}_m = \frac{2}{\pi c_m} \int_{-1}^{1} f(x) T_m(x) (1 - x^2)^{-1/2} dx,$$

where $c_m = 2$ if m = 0, or 1 if $m \ge 1$. The discrete form of the Chebyshev polynomials is commonly described on the set of Gauss-Lobatto collocation points n_i , ranging from 1 to -1, given by

$$n_j = \cos\left(\frac{\pi j}{N}\right), \quad 0 \le j \le N.$$

The discrete Chebyshev polynomials of the first kind $T_{m,j}$ and the interpolated function f_j , on the collocation points n_j , are defined as

$$T_{m,j} = \cos\left(\frac{m\pi j}{N}\right), \quad f_j = \sum_{m=0}^{N} \hat{f}_m T_{m,j}.$$

The derivative of the interpolated function at the collocation points can simply be expressed by matrix multiplication, such that

$$\left(\frac{\mathrm{d}f}{\mathrm{d}x}\right)_{j} = \sum_{l=0}^{N} (D_{N})_{j,l} f_{l},$$

where the entries of D_N are deduced from the derivative of the Chebyshev polynomials of the first kind (see Ref [61]. Chapter 2.4). This gives

$$(D_N)_{j,l} = \left\{ \begin{array}{ll} \frac{c_j}{c_l} \frac{(-1)^{j+l}}{n_j - n_l}, & \text{if} \quad j \neq l, \\ \frac{-n_l}{2(1 - n_l^2)}, & \text{if} \quad 1 \leq j = l \leq N - 1, \\ \frac{2N^2 + 1}{6}, & \text{if} \quad j = l = 0, \\ -\frac{2N^2 + 1}{6}, & \text{if} \quad j = l = N, \end{array} \right.$$

where

$$c_j = \left\{ \begin{array}{ll} 2, & \text{if} \quad j=0,\,N,\\ 1, & \text{if} \quad 1 \leq j \leq N-1. \end{array} \right.$$

The second derivative can be computed from the square of the matrix D_N . Finally, in order to account for the metric of the physical space, the collocation points n_i and the derivative matrix D_N are scaled by a factor -h(S)/2. This gives

$$n_j^* = \frac{-h(S)}{2} n_j, \quad (D_N^*)_{j,l} = \frac{-2}{h(S)} (D_N)_{j,l}, \quad \forall (j,l).$$
(B.3)

Each equation in (B.1) is described by a matrix in its discrete form. The boundary conditions are then applied through the first and last lines of each sub-matrix, which correspond to the boundary points. For the second equation, $\psi^* = \mu \psi$, there is no need for boundary conditions. Hence, the first and last lines are discarded and the vector ψ^* is only evaluated on N-1 collocation points, i.e. the inner collocation points $1 \le i \le N-1$. For the first equation (the mode shape equation), the first and last lines are replaced by the boundary conditions, Eq. (27) in discrete form, which reads

$$\sum_{l=0}^{N} (D_N^*)_{j,l} \psi_l = 0, \quad j = 0, N.$$

The generalized eigenvalue problem (B.1) is finally written in discrete form as

$$\begin{bmatrix} \underline{\mathcal{L}} & \underline{\mathbf{O}} \\ \underline{\mathbf{O}} & \underline{\mathbf{I}} \end{bmatrix} \begin{bmatrix} \psi \\ \psi^* \end{bmatrix} = \begin{bmatrix} \underline{\mathbf{M}}_1 & \underline{\mathbf{M}}_2 \\ \Psi^* \end{bmatrix} \begin{bmatrix} \psi \\ \psi^* \end{bmatrix} \underline{\mu}, \tag{B.4}$$

where

$$[\mathcal{L}]_{j,l} = \left\{ \begin{array}{ll} (D_N^{*2})_{j,l} + (D_N^*)_{j,l} / (R_c + n_j^*) + k^2, & \text{if} \quad 1 \leq j \leq N-1, \\ (D_N^*)_{j,l}, & \text{if} \quad j = 0, \, N, \end{array} \right.$$

$$\begin{bmatrix} M_1 \end{bmatrix}_{j,l} = \left\{ \begin{array}{ll} 2kM/(1+n_j^*/R_c)\delta_{j,l}, & \text{if} \quad 1 \leq j \leq N-1, \\ 0, & \text{if} \quad j = 0, N, \end{array} \right.$$

$$\left[M_{2}\right]_{j,i} = \left\{ \begin{array}{ll} \beta^{2}/(1+n_{j}^{*}/R_{c})^{2}\delta_{j,i}, & \text{if} \quad 1 \leq j \leq N-1, \\ 0, & \text{if} \quad j = 0, N, \end{array} \right.$$

 δ denoting the Kronecker delta, $1 \le i \le N-1$ and $0 \le l \le N$. The discrete eigenvalue problem (B.4) is solved at each location S by employing a built-in solver in Matlab using the QZ algorithm (*eig* function), which returns the desired eigenfunctions $\psi_l(S, n_j^*)$ and their associated eigenvalues $\mu_l(S)$.

Appendix C. Mode-matching equations at the staggered leading-edge interface

C.1. Continuity of the acoustic potential

To derive the matching equations, a change of variables is performed on the channel modes to express all potentials in terms of (x, y). For the potential ϕ_d , it yields

$$\phi_{d}(x,y) = \frac{1}{2} \sum_{q=0}^{\infty} A_{q} \left[e^{i\left(-\frac{q\pi}{a}\sin\Psi + k_{q}^{+}\cos\Psi\right)x} e^{i\left(\frac{q\pi}{a}\cos\Psi + k_{q}^{+}\sin\Psi\right)y} + e^{i\left(\frac{q\pi}{a}\sin\Psi + k_{q}^{+}\cos\Psi\right)x} e^{i\left(-\frac{q\pi}{a}\cos\Psi + k_{q}^{+}\sin\Psi\right)y} \right]. \tag{C.1}$$

For the sake of brevity, the potential ϕ_u is written with the coefficients \tilde{B}_q as in Eq. (43) in the following. The acoustic potential continuity at the leading-edge interface reads

$$\begin{split} &\frac{1}{2}\sum_{q=0}^{\infty}A_{q}\left[\mathrm{e}^{\mathrm{i}\left(\frac{q\pi}{b}+k_{q}^{+}\sin\Psi\right)y}+\mathrm{e}^{\mathrm{i}\left(-\frac{q\pi}{b}+k_{q}^{+}\sin\Psi\right)y}\right]+\tilde{B}_{q}\left[\mathrm{e}^{\mathrm{i}\left(\frac{q\pi}{b}+k_{q}^{-}\sin\Psi\right)y}+\mathrm{e}^{\mathrm{i}\left(-\frac{q\pi}{b}+k_{q}^{-}\sin\Psi\right)y}\right]\mathrm{e}^{-\mathrm{i}k_{q}^{-}b\sin\Psi}\\ &=\sum_{p=-\infty}^{\infty}R_{p}\mathrm{e}^{\mathrm{i}\alpha_{p}y}+\mathrm{e}^{\mathrm{i}\alpha_{j}y}. \end{split} \tag{C.2}$$

The projection on the annular modal basis is performed with the operator

$$\int_0^b (\bullet) e^{-i\alpha_p y} dy, \quad \text{with} \quad \alpha_p = \alpha_j + p \frac{2\pi}{b}, \ p \in \mathbb{Z}.$$

This leads to

$$\sum_{n=0}^{\infty} A_q \left(\Im_{q,p}^{++} + \Im_{q,p}^{-+} \right) + \tilde{B}_q \left(\Im_{q,p}^{+-} + \Im_{q,p}^{--} \right) e^{-ik_q^- b \sin \Psi} = b \left(R_p + \delta_{p,0} \right), \tag{C.3}$$

where the integrals on the staggered channel modes are defined by

$$\mathfrak{I}_{q,p}^{\pm\pm} = \frac{1}{2} \int_{0}^{b} \mathrm{e}^{\mathrm{i}(\pm\frac{q\pi}{b} + k_{q}^{\pm} \sin\Psi - \alpha_{p})y} \, \mathrm{d}y = \frac{b}{2} \frac{\sin\left(\varphi_{q,p}^{\pm\pm}\right)}{\varphi_{q,p}^{\pm\pm}} \mathrm{e}^{\mathrm{i}\varphi_{q,p}^{\pm\pm}},$$

with

$$\varphi_{q,p}^{\pm\pm} = \frac{b}{2} \left(\pm \frac{q\pi}{b} + k_q^{\pm} \sin \Psi - \alpha_p \right).$$

The integrals can also be recast together in the potential continuity Eq. (C.3) to give the result of Eq. (50) as

$$\sum_{q=0}^{\infty} A_q \mathfrak{I}_{q,p}^+ + \tilde{B}_q \mathfrak{I}_{q,p}^- e^{-ik_q^- b \sin \Psi} = b \left(R_p + \delta_{p,0} \right), \tag{C.4}$$

where

$$\mathfrak{I}_{q,p}^{\pm}(\boldsymbol{\Psi}) = \mathfrak{I}_{q,p}^{+\pm} + \mathfrak{I}_{q,p}^{-\pm} = \begin{cases}
\frac{-\mathrm{i}(k_q^{\pm}\sin\boldsymbol{\Psi} - \alpha_p)}{(q\pi/b)^2 - (k_q^{\pm}\sin\boldsymbol{\Psi} - \alpha_p)^2} \left(1 - (-1)^q \mathrm{e}^{\mathrm{i}b(k_q^{\pm}\sin\boldsymbol{\Psi} - \alpha_p)}\right), \\
\frac{b}{2} \left(1 + \delta_{q,0}\right) & \text{if} \quad \left|k_q^{\pm}\sin\boldsymbol{\Psi} - \alpha_p\right| = \frac{q\pi}{b}.
\end{cases}$$
(C.5)

C.2. Continuity of the modified acoustic velocity

To write the continuity equation on the modified acoustic velocity $\beta_x^2 u_x - M_x M_y u_y$, the derivatives of the potential (C.1) with respect to each coordinate are needed. They are derived as

$$\frac{\partial \phi_d}{\partial x} = \frac{i}{2} \sum_{q=0}^{\infty} A_q \left[\left(-\frac{q\pi}{a} \sin \Psi + k_q^+ \cos \Psi \right) e^{i \left(-\frac{q\pi}{a} \sin \Psi + k_q^+ \cos \Psi \right) x} e^{i \left(\frac{q\pi}{a} \cos \Psi + k_q^+ \sin \Psi \right) y} \right. \\
\left. + \left(\frac{q\pi}{a} \sin \Psi + k_q^+ \cos \Psi \right) e^{i \left(\frac{q\pi}{a} \sin \Psi + k_q^+ \cos \Psi \right) x} e^{i \left(-\frac{q\pi}{a} \cos \Psi + k_q^+ \sin \Psi \right) y} \right], \tag{C.6}$$

and

$$\begin{split} \frac{\partial \phi_d}{\partial y} &= \frac{\mathrm{i}}{2} \sum_{q=0}^{\infty} A_q \left[\left(\frac{q\pi}{a} \cos \Psi + k_q^+ \sin \Psi \right) \mathrm{e}^{\mathrm{i} \left(-\frac{q\pi}{a} \sin \Psi + k_q^+ \cos \Psi \right) x} \mathrm{e}^{\mathrm{i} \left(\frac{q\pi}{a} \cos \Psi + k_q^+ \sin \Psi \right) y} \right. \\ &+ \left. \left(-\frac{q\pi}{a} \cos \Psi + k_q^+ \sin \Psi \right) \mathrm{e}^{\mathrm{i} \left(\frac{q\pi}{a} \sin \Psi + k_q^+ \cos \Psi \right) x} \mathrm{e}^{\mathrm{i} \left(-\frac{q\pi}{a} \cos \Psi + k_q^+ \sin \Psi \right) y} \right]. \end{split} \tag{C.7}$$

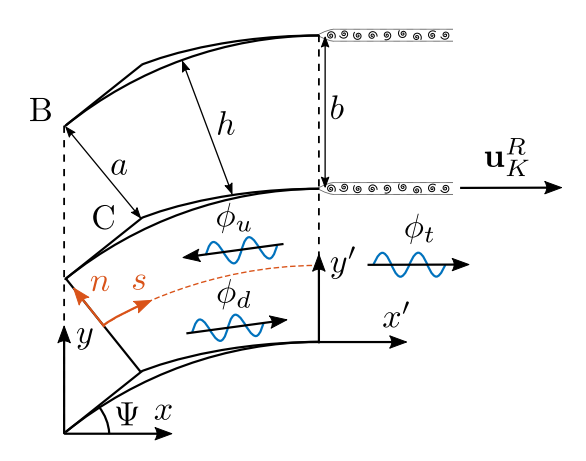


Fig. D.28. Scattering of a downstream-propagating channel mode at the trailing-edge interface with infinitely thin vorticity sheets induced by the Kutta condition.

The modified velocity continuity at the leading-edge interface reads

$$\begin{split} &\frac{1}{2} \sum_{q=0}^{\infty} A_{q} \left[\left(\beta_{x}^{2} K_{q}^{+-} - M_{x} M_{y} A_{q}^{++} \right) e^{\mathrm{i} A_{q}^{++} y} + \left(\beta_{x}^{2} K_{q}^{++} - M_{x} M_{y} A_{q}^{-+} \right) e^{\mathrm{i} A_{q}^{-+} y} \right] \\ &+ \tilde{B}_{q} \left[\left(\beta_{x}^{2} K_{q}^{--} - M_{x} M_{y} A_{q}^{+-} \right) e^{\mathrm{i} A_{q}^{+-} y} + \left(\beta_{x}^{2} K_{q}^{-+} - M_{x} M_{y} A_{q}^{--} \right) e^{\mathrm{i} A_{q}^{--} y} \right] e^{-\mathrm{i} k_{q}^{-} b \sin \Psi} \\ &= \sum_{n=-\infty}^{\infty} R_{p} \left(\beta_{x}^{2} k_{p}^{-} - M_{x} M_{y} \alpha_{p} \right) e^{\mathrm{i} \alpha_{p} y} + \left(\beta_{x}^{2} k_{j}^{+} - M_{x} M_{y} \alpha_{j} \right) e^{\mathrm{i} \alpha_{j} y}, \end{split}$$
 (C.8)

where

$$K_q^{\pm\pm} = k_q^\pm \cos \Psi \pm \frac{q\pi}{a} \sin \Psi, \quad A_q^{\pm\pm} = \pm \frac{q\pi}{a} \cos \Psi + k_q^\pm \sin \Psi.$$

Using the same projection method as previously gives the result of Eq. (51) as

$$\sum_{q=0}^{\infty} A_q \mathcal{K}_{q,p}^+ \mathcal{I}_{q,p}^+ + \tilde{B}_q \mathcal{K}_{q,p}^- \mathcal{I}_{q,p}^- e^{-ik_q^- b \sin \Psi} = b \left(\mathcal{K}_p^- R_p + \mathcal{K}_j^+ \delta_{p,0} \right), \tag{C.9}$$

where the staggered axial wavenumbers are defined by

$$\begin{split} \mathcal{K}_{j}^{+} &= \beta_{x}^{2} k_{j}^{+} - M_{x} M_{y} \alpha_{j}, \\ \mathcal{K}_{p}^{-} &= \beta_{x}^{2} k_{p}^{-} - M_{x} M_{y} \alpha_{p}, \\ \mathcal{K}_{q,p}^{\pm} &= \left(\beta_{x}^{2} \cos \Psi - M_{x} M_{y} \sin \Psi\right) k_{q}^{\pm} + \frac{\tan \Psi}{k_{q}^{\pm} \sin \Psi - \alpha_{p}} \left(\frac{q\pi}{b}\right)^{2}. \end{split}$$

Appendix D. Implementation of a Kutta condition

In the presence of an inviscid mean flow, a Kutta condition is needed on the fluctuating variables of the mode-matching model. This condition enforces a finite velocity at the trailing edges, allowing to indirectly account for some viscous effects within an inviscid flow. According to Rienstra [62], this condition is equivalently expressed by enforcing a zero pressure jump at the trailing edge of the vanes. This has for consequence the generation of a vortex shedding from the edges, which is modeled by infinitely thin vortical sheets convected at the speed of the mean flow [63]. This adds a vortical velocity field \mathbf{u}_K^R downstream of the vanes, that has to be accounted for in the matching equations. The new problem to solve at the trailing-edge interface is depicted in Fig. D.28.

The zero pressure jump at the trailing edge, between a reference channel (p^0) and the channel below (p^{-1}) , is derived as

$$\begin{split} p^{-1}(S &= L_c, n = b/2) = p^0(S = L_c, n = -b/2), \\ \Leftrightarrow \sum_{q=0}^{\infty} \sum_{l=0}^{\infty} \sum_{q^*=0}^{\infty} \left[A_q \mathrm{e}^{\mathrm{i} k_q^+ a \tan \Psi} B_l^q(0) Y_l^+ \left(k \mathcal{A}_{q^*}^l(L_c) - M \mu_l^+ \tilde{\mathcal{A}}_{q^*}^l(L_c) \right) \right. \\ &\left. + B_q B_l^q(L_c) \left(k \mathcal{A}_{q^*}^l(L_c) - M \mu_l^- \tilde{\mathcal{A}}_{q^*}^l(L_c) \right) \right] \cos(q^* \pi) \mathrm{e}^{-\mathrm{i} \alpha_j b} \\ &= \sum_{q=0}^{\infty} \sum_{l=0}^{\infty} \sum_{q^*=0}^{\infty} \left[A_q \mathrm{e}^{\mathrm{i} k_q^+ a \tan \Psi} B_l^q(0) Y_l^+ \left(k \mathcal{A}_{q^*}^l(L_c) - M \mu_l^+ \tilde{\mathcal{A}}_{q^*}^l(L_c) \right) \right] \end{split}$$

$$+B_q\mathcal{B}_l^q(L_c)\left(k\mathcal{A}_{q^*}^l(L_c)-M\mu_l^-\tilde{\mathcal{A}}_{q^*}^l(L_c)\right)\right],$$

which can be rewritten as

$$\begin{split} &\sum_{q=0}^{\infty}\sum_{l=0}^{\infty}\sum_{q^*=0}^{\infty}A_q\mathrm{e}^{\mathrm{i}k_q^+a\tan^{\Psi}}\mathcal{B}_l^q(0)Y_l^+\left(k\mathcal{A}_{q^*}^l(L_c)-M\mu_l^+\tilde{\mathcal{A}}_{q^*}^l(L_c)\right)\left(1-(-1)^{q^*}\mathrm{e}^{-\mathrm{i}\alpha_jb}\right)\\ &=-\sum_{q=0}^{\infty}\sum_{l=0}^{\infty}\sum_{q^*=0}^{\infty}B_q\mathcal{B}_l^q(L_c)\left(k\mathcal{A}_{q^*}^l(L_c)-M\mu_l^-\tilde{\mathcal{A}}_{q^*}^l(L_c)\right)\left(1-(-1)^{q^*}\mathrm{e}^{-\mathrm{i}\alpha_jb}\right). \end{split} \tag{D.1} \\ &\text{Since the vanes are locally aligned with the turbomachinery axis at the trailing edge, the vortical sheets are the same as for} \end{split}$$

unstaggered flat vanes. Hence, the velocity field \mathbf{u}_{K}^{R} is described as [6]

$$\mathbf{u}_{K}^{R}(x', y') = \sum_{p=-\infty}^{\infty} \mathbf{U}_{p}^{R} e^{i\alpha_{p} y'} e^{i(k/M)x'}, \quad 0 \le x' < \infty, \quad 0 \le y' < 2\pi R,$$
(D.2)

$$\mathbf{U}_{p}^{R} = \frac{\mathrm{i}\Omega_{K}}{b} \frac{\left[\alpha_{p} \mathbf{e}_{x} - (k/M)\mathbf{e}_{y}\right]}{\alpha_{p}^{2} + (k/M)^{2}},\tag{D.3}$$

where Ω_K is the unknown amplitude of the associated vortical field. Due to the presence of the vortical field, the total velocity field is not potential anymore downstream of the cascade. Thus, the continuity of the fluctuating velocity potential ϕ no longer enforces the continuity of the total enthalpy (A.7). The trailing-edge matching equations with a Kutta condition are then expressed on the set of variables (p, u_x) . The velocity field \mathbf{u}_k^R being pressure-free, the continuity of the fluctuating pressure p is given by

$$\sum_{q=0}^{\infty} \sum_{l=0}^{\infty} \left[A_{q} e^{ik_{q}^{+}b \sin \Psi} \mathcal{B}_{l}^{q}(0) Y_{l}^{+} \left(k \mathcal{A}_{q^{*}}^{l}(L_{c}) - M \mu_{l}^{+} \tilde{\mathcal{A}}_{q^{*}}^{l}(L_{c}) \right) + B_{q} \mathcal{B}_{l}^{q}(L_{c}) \left(k \mathcal{A}_{q^{*}}^{l}(L_{c}) - M \mu_{l}^{-} \tilde{\mathcal{A}}_{q^{*}}^{l}(L_{c}) \right) \right] \Im_{q^{*},p}^{0} = b(k - M k_{p}^{+}) T_{p}.$$
(D.4)

On the other hand, the continuity of the fluctuating axial velocity u_x with the Kutta condition yields

$$\begin{split} &\sum_{q=0}^{\infty} \sum_{l=0}^{\infty} \sum_{q^*=0}^{\infty} \left[A_q e^{ik_q^+ b \sin \Psi} \mathcal{B}_l^q(0) \mu_l^+ Y_l^+ + B_q \mathcal{B}_l^q(L_c) \mu_l^- \right] \tilde{\mathcal{A}}_{q^*}^l(L_c) \mathcal{I}_{q^*,p}^0 \\ &= b k_p^+ T_p + \frac{\alpha_p}{\alpha_p^2 + (k/M)^2} \Omega_K. \end{split} \tag{D.5}$$

Data availability

Data will be made available on request.

References

- //dx.doi.org/10.2514/6.2007-3728.
- E.A.N. Whitehead, The theory of parallel-plate media for microwave lenses, in: Proceedings of the IEE Part III: Radio and Communication Engineering, vol. 98, 1951, pp. 133–140, http://dx.doi.org/10.1049/pi-3.1951.0025.
- [3] R. Mittra, S.W. Lee, Analytical Techniques in the Theory of Guided Waves, Macmillan, 1971.
- S. Kaji, T. Okazaki, Propagation of sound waves through a blade row: II. Analysis based on the acceleration potential method, J. Sound Vib. 11 (1970) 355-375, http://dx.doi.org/10.1016/S0022-460X(70)80039-6.
- [5] W. Koch, On the transmission of sound waves through a blade row, J. Sound Vib. 18 (1971) 111-128, http://dx.doi.org/10.1016/0022-460X(71)90635-3.
- [6] S. Bouley, B. François, M. Roger, H. Posson, S. Moreau, On a two-dimensional mode-matching technique for sound generation and transmission in axial-flow outlet guide vanes, J. Sound Vib. 403 (2017) 190-213, http://dx.doi.org/10.1016/j.jsv.2017.04.031.
- M. Roger, Analytical modelling of wake-interaction noise in centrifugal compressors with vaned diffusers, in: 10th AIAA/CEAS Aeroacoustics Conference, Manchester, Great Britain, 2004, http://dx.doi.org/10.2514/6.2004-2994.
- J. Ingenito, M. Roger, Analytical modelling of sound transmission through the passage of centrifugal compressors, in: 13th AIAA/CEAS Aeroacoustics Conference, Rome, Italy, 2007, http://dx.doi.org/10.2514/6.2007-3704.
- J. Ingenito, M. Roger, Measurement and prediction of the tonal noise of a centrifugal compressor at inlet, in: 15th AIAA/CEAS Aeroacoustics Conference, Miami, FL, USA, 2009, http://dx.doi.org/10.2514/6.2009-3360.
- [10] M. Roger, S. Moreau, A. Marsan, Generation and transmission of spiral acoustic waves in multi-stage subsonic radial compressors, in: 20th AIAA/CEAS Aeroacoustics Conference, Atlanta, GA, USA, 2014, http://dx.doi.org/10.2514/6.2014-3232.
- [11] S. Bouley, B. François, M. Roger, On a mode-matching technique for sound generation and transmission in a three-dimensional annular cascade of outlet guide vanes, in: 22nd AIAA/CEAS Aeroacoustics Conference, Lyon, France, 2016, http://dx.doi.org/10.2514/6.2016-2880.
- B. François, S. Bouley, M. Roger, S. Moreau, Analytical models based on a mode-matching technique for turbulence impingement noise on axial-flow outlet guide vanes, in: 22nd AIAA/CEAS Aeroacoustics Conference, Lyon, France, 2016, http://dx.doi.org/10.2514/6.2016-2947.
- S. Bouley, A. Finez, M. Roger, Rotor-stator wake-interaction tonal noise modeling with an edge-dipole approach, in: 22nd AIAA/CEAS Aeroacoustics Conference, Lyon, France, 2016, http://dx.doi.org/10.2514/6.2016-3061.
- [14] M. Roger, B. François, M. Bauerheim, Three-dimensional modeling of annular cascade trailing-edge noise, in: 22nd AIAA/CEAS Aeroacoustics Conference, Lyon, France, 2016, http://dx.doi.org/10.2514/6.2016-2949.
- M. Roger, B. François, S. Moreau, Cascade trailing-edge noise modeling using a mode-matching technique and the edge-dipole theory, J. Sound Vib. 382 (2016) 310-327, http://dx.doi.org/10.1016/j.jsv.2016.06.035.

- [16] M. Roger, B. François, Combined analytical models for sound generation and transmission in cambered axial-flow outlet guide vanes, Eur. J. Mech. B Fluids 61 (2017) 218–225, http://dx.doi.org/10.1016/j.euromechflu.2016.10.006.
- [17] M. Roger, S. Moreau, Coupled mode-matching and slowly-varying duct formulations for predicting noise generation and transmission in axial-flow rotor-stator stages, in: MUSAF III, Toulouse, France, 2016.
- [18] R. Hixon, Computational aeroacoustics prediction of acoustic transmission through a realistic 2D stator, in: 17th AIAA/CEAS Aeroacoustics Conference, Portland, Oregon, 2011, http://dx.doi.org/10.2514/6.2011-2706.
- [19] P.J. Baddoo, L.J. Ayton, An analytic solution for gust-cascade interaction noise including effects of realistic aerofoil geometry, J. Fluid Mech. 886 (2020) http://dx.doi.org/10.1017/jfm.2019.1016.
- [20] S. Moreau, P. Baddoo, H. Bériot, M. Roger, Two-dimensional sound transmission in realistic turbomachinery cascade, in: 25th AIAA/CEAS Aeroacoustics Conference. Delft. The Netherlands. 2019. http://dx.doi.org/10.2514/6.2019-2550.
- [21] N.C. Ovenden, A uniformly valid multiple scales solution for cut-on cut-off transition of sound in flow ducts, J. Sound Vib. 286 (2005) 403–416, http://dx.doi.org/10.1016/j.jsv.2004.12.009.
- [22] Y. Mao, A.G. Wilson, P. Joseph, P. Chaitanya, A. Parry, P. Carugno, Wave response functions for a cascade of blades with an arbitrary camber, in: 25th AIAA/CEAS Aeroacoustics Conference, Delft, The Netherlands, 2019, http://dx.doi.org/10.2514/6.2019-2736.
- [23] I. Evers, N. Peake, On sound generation by the interaction between turbulence and a cascade of airfoils with non-uniform mean flow, J. Fluid Mech. 463 (2002) 25–52, http://dx.doi.org/10.1017/S0022112002008698.
- [24] J. de Laborderie, S. Moreau, A. Berry, H. Posson, Several technological effects on tonal fan noise prediction, in: 18th AIAA/CEAS Aeroacoustics Conference (33rd AIAA Aeroacoustics Conference), Colorado Springs, CO, 2012, http://dx.doi.org/10.2514/6.2012-2131.
- [25] J. de Laborderie, S. Moreau, Evaluation of a cascade-based acoustic model for fan tonal noise prediction, AIAA J. 52 (2014) 2877–2890, http://dx.doi.org/10.2514/1.J053008.
- [26] J. de Laborderie, V. Blandeau, T. Node-Langlois, S. Moreau, Extension of a fan tonal noise cascade model for camber effects, AIAA J. 53 (2015) 863–876, http://dx.doi.org/10.2514/1.J053266.
- [27] P. Chaitanya, J. Coupland, P. Joseph, Airfoil geometry effects on turbulence interaction noise in cascades, in: 22nd AIAA/CEAS Aeroacoustics Conference, Lyon, France, 2016, http://dx.doi.org/10.2514/6.2016-2738.
- [28] F. Gea-Aguilera, J. Gill, X. Zhang, On the effects of fan wake modelling and vane design on cascade noise, J. Sound Vib. 459 (2019) 114859, http://dx.doi.org/10.1016/j.isv.2019.114859
- [29] M. Sanjosé, M. Daroukh, W. Magnet, J. De Laborderie, S. Moreau, A. Mann, Tonal fan noise prediction and validation on the ANCF configuration, in:

 Proceedings of the International Conference on Fan Noise, Technology and Numerical Methods, Lyon, France, 2015.
- [30] S.M. Grace, Fan broadband interaction noise modeling using a low-order method, J. Sound Vib. 346 (2015) 402–423, http://dx.doi.org/10.1016/j.jsv. 2015.02.013.
- [31] D. Lewis, J. de Laborderie, M. Sanjosé, S. Moreau, M.C. Jacob, V. Masson, Parametric study on state-of-the-art analytical models for fan broadband interaction noise predictions, J. Sound Vib. 514 (2021) http://dx.doi.org/10.1016/j.jsv.2021.116423.
- [32] N. Curle, The influence of solid boundaries upon aerodynamic sound, Proc. R. Soc. Lond. Ser. A. Mathematical Phys. Sci. 231 (1955) 505–514, http://dx.doi.org/10.1098/rspa.1955.0191.
- [33] N. Peake, E.J. Kerschen, Influence of mean loading on noise generated by the interaction of gusts with a flat-plate cascade: upstream radiation, J. Fluid Mech. 347 (1997) 315–346, http://dx.doi.org/10.1017/S0022112097006502.
- [34] N. Peake, E.J. Kerschen, Influence of mean loading on noise generated by the interaction of gusts with a cascade: downstream radiation, J. Fluid Mech. 515 (2004) 99–133, http://dx.doi.org/10.1017/S0022112004000618.
- [35] E.J. Brambley, N. Peake, Sound transmission in strongly curved slowly varying cylindrical ducts with flow, J. Fluid Mech. 596 (2008) 387–412, http://dx.doi.org/10.1017/S0022112007009603.
- [36] S.L. Dixon, C.A. Hall, Fluid Mechanics and Thermodynamics of Turbomachinery, Seventh ed., Elsevier, 2014.
- [37] A.H. Nayfeh, D.P. Telionis, Acoustic propagation in ducts with varying cross sections, J. Acoust. Soc. Am. 54 (1973) 1654–1661, http://dx.doi.org/10.
- [38] A.H. Nayfeh, D.P. Telionis, S.G. Lekoudis, Acoustic propagation in ducts with varying cross sections and sheared mean flow, in: Aeroacoustics Conference, Seattle, WA, USA, 1973, http://dx.doi.org/10.2514/6.1973-1008.
- [39] A.H. Nayfeh, J.E. Kaiser, D.P. Telionis, Transmission of sound through annular ducts of varying cross sections, AIAA J. 13 (1975) 60–65, http://dx.doi.org/10.2514/3.49631.
- [40] S.W. Rienstra, Contributions to the theory of sound propagation in ducts with bulk-reacting lining, J. Acoust. Soc. Am. 77 (1985) 1681–1685, http://dx.doi.org/10.1121/1.391914.
- [41] S.W. Rienstra, Sound transmission in a slowly varying lined flow duct, Nieuw Arch. Voor Wiskd. 4/6 (1988) 157-167.
- [42] S.W. Rienstra, Sound transmission in slowly varying circular and annular lined ducts with flow, J. Fluid Mech. 380 (1999) 279–296, http://dx.doi.org/10.1017/S0022112098003607.
- [43] S.W. Rienstra, Sound propagation in slowly varying lined flow ducts of arbitrary cross-section, J. Fluid Mech. 495 (2003) 157–173, http://dx.doi.org/10. 1017/S0022112003006050.
- [44] S.W. Rienstra, Slowly varying modes in a two-dimensional duct with shear flow and lined walls, J. Fluid Mech. 906 (2021) http://dx.doi.org/10.1017/ ifm.2020.687.
- [45] S.W. Rienstra, W. Eversman, A numerical comparison between the multiple-scales and finite-element solution for sound propagation in lined flow ducts, J. Fluid Mech. 437 (2001) 367–384, http://dx.doi.org/10.1017/S0022112001004438.
- [46] B. Mangin, M. Daroukh, G. Gabard, Propagation of acoustic waves in ducts with flow using the multimodal formulation, AIAA J. 61 (2023) 2721–2733, http://dx.doi.org/10.2514/1.J062659.
- [47] M.D. Dahl (Ed.), Fourth Computational Aeroacoustics (CAA) Workshop on Benchmark Problems, (NASA/CP-2004-212954) NASA, 2004.
- [48] C. Bender, S. Orszag, Advanced Mathematical Methods for Scientists and Engineers, McGraw-Hill, 1978.
- [49] M.H. Holmes, Introduction to Perturbation Methods, Springer-Verlag, 1995.
- [50] P.E. Krasnushkin, On waves in curved tubes, Uchenye Zap. Mosk. Gos. Univ. 75 (1945) 9-27.
- [51] L. Girier, M. Roger, H. Bériot, A. Lafitte, H. Posson, A two-dimensional model of sound transmission through curved and staggered OGV: Effect of inter-vane channel mode transitions, in: 25th AIAA/CEAS Aeroacoustics Conference, Delft, The Netherlands, 2019, http://dx.doi.org/10.2514/6.2019-2690.
- [52] A.D. Pierce, Acoustics: An Introduction to Its Physical Principles and Applications, McGraw-Hill, 1981.
- [53] S. Felix, V. Pagneux, Sound propagation in rigid bends: A multimodal approach, J. Acoust. Soc. Am. 110 (2001) 1329–1337, http://dx.doi.org/10.1121/ 1.1391249.
- [54] B. François, S. Bouley, H. Posson, M. Roger, On the kutta condition for the sound transmission through outlet guide vanes, in: Congrès Français de Mécanique, CFM, Lyon, France, 2015.
- [55] C.J. Chapman, Sound radiation from a cylindrical duct. Part 1. Ray structure of the duct modes and of the external field, J. Fluid Mech. 281 (1994) 293–311, http://dx.doi.org/10.1017/S0022112094003113.
- [56] H. Bériot, A. Prinn, G. Gabard, Efficient implementation of high-order finite elements for Helmholtz problems, Internat. J. Numer. Methods Engrg. 106 (2016) 213–240, http://dx.doi.org/10.1002/nme.5172.

- [57] H. Bériot, G. Gabard, Anisotropic adaptivity of the p-FEM for time-harmonic acoustic wave propagation, J. Comput. Phys. 378 (2019) 234–256, http://dx.doi.org/10.1016/j.jcp.2018.11.013.
- [58] H. Bériot, A. Modave, An automatic perfectly matched layer for acoustic finite element simulations in convex domains of general shape, Internat. J. Numer. Methods Engrg. 122 (2021) 1239–1261, http://dx.doi.org/10.1002/nme.6560.
- [59] G. Podboy, M. Krupar, C. Hughes, R. Woodward, Fan noise source diagnostic test- LDV measured flow field results, in: 8th AIAA/CEAS Aeroacoustics Conference & Exhibit, Breckenridge, Colorado, USA, 2002, http://dx.doi.org/10.2514/6.2002-2431.
- [60] J.M. Janus, H.Z. Horstman, D.L. Whitfield, Unsteady flowfield simulation of ducted prop-fan configurations, in: 30th Aerospace Sciences Meeting and Exhibit, Reno, NV, USA, 1992, http://dx.doi.org/10.2514/6.1992-521.
- [61] C. Canuto, M.Y. Hussaini, A. Quarteroni, T.A. Zang, Spectral Methods in Fluid Dynamics, Springer-Verlag, 1988.
- [62] S.W. Rienstra, Sound diffraction at a trailing edge, J. Fluid Mech. 108 (1981) 443–460, http://dx.doi.org/10.1017/S0022112081002206.
- [63] M.S. Howe, Attenuation of sound due to vortex shedding from a splitter plate in a mean flow duct, J. Sound Vib. 105 (1986) 385–396, http://dx.doi.org/10.1016/0022-460X(86)90167-7.